J. Fluid Mech. (2000), *vol.* 410, *pp.* 29–65. Printed in the United Kingdom

Dynamics and low-dimensionality of a turbulent near wake

By X. MA, G.-S. KARAMANOS AND G. E. KARNIADAKIS
Division of Applied Mathematics, Brown University, Providence, RI 02912, USA

(Received 19 May 1998 and in revised form 12 November 1999)

We investigate the dynamics of the near wake in turbulent flow past a circular cylinder up to ten cylinder diameters downstream. The very near wake (up to three diameters) is dominated by the shear layer dynamics and is very sensitive to disturbances and cylinder aspect ratio. We perform systematic spectral direct (DNS) and large-eddy simulations (LES) at Reynolds number (Re) between 500 and 5000 with resolution ranging from 200 000 to 100 000 000 degrees of freedom. In this paper, we analyse in detail results at $Re = 3900$ and compare them to several sets of experiments. Two converged states emerge that correspond to a U-shape and a V-shape mean velocity profile at about one diameter behind the cylinder. This finding is consistent with the experimental data and other published LES. Farther downstream, the flow is dominated by the vortex shedding dynamics and is not as sensitive to the aforementioned factors. We also examine the development of a turbulent state and the inertial subrange of the corresponding energy spectrum in the near wake. We find that an inertial range exists that spans more than half a decade of wavenumber, in agreement with the experimental results. In contrast, very low-resolution spectral simulation as well as other dissipative LES do not describe accurately the inertial range although they predict low-order statistics relatively accurately. This finding is analysed in the context of coherent structures using a phase averaging technique and a procedure to extract the most energetic (on the average) eigenmodes of the flow. The results suggest that a dynamical model would require of the order of twenty modes to describe the vortex shedding dynamics with reasonable accuracy.

1. Introduction

1.1. *Background*

The near wake of incompressible flow past a circular cylinder is a very critical region as it determines the dominant instability in the flow, i.e. the absolute instability that leads to the vortex street formation, see Triantafyllou, Triantafyllou & Chryssostomidis (1986), Unal & Rockwell (1988), Monkewitz (1988), Karniadakis & Triantafyllou (1989), in both laminar and turbulent wakes. This was shown by Triantafyllou *et al.* (1986), who demonstrated that such instability exists even in the turbulent regime by analysing the experimental time-averaged velocity data of Cantwell & Coles (1983) for Reynolds number $Re = 140\,000$. The near wake is also responsible for the secondary instability as well as subsequent bifurcations that lead to a turbulent state, as found in experimental work, see Williamson (1996), Hammache & Gharib (1991), Eisenlohr & Eckelmann (1989), and in numerical work, see Karniadakis & Triantafyllou (1992), Barkley & Henderson (1996), Robichaux, Balachandar & Vanka (1999).

Of particular physical importance is the dynamics of the two shear layers developing

on the two sides of the cylinder. Experimental evidence suggests that there is a rather wide Reynolds number range within which a shear layer instability may occur, from $Re_c \approx 350$ (due to Gerrard 1978) to $Re_c \approx 3000$ (due to Wu *et al.* 1996). The prevailing hypothesis has been that background disturbances strongly influence the critical Reynolds number value Re_c (Unal & Rockwell 1988). However, other factors such as the aspect ratio (cylinder diameter to spanwise length), the end conditions, and even the shedding mode, e.g. parallel or oblique, can influence Re_c (Prasad & Williamson 1997). Unlike the classical shear layers of two co-flowing streams (Huang & Ho 1990), the cylinder shear layers are restricted in the streamwise direction by the formation of large-scale Kármán vortices. In particular, the cylinder shear layers have an upstream effect due to the aforementioned absolute instability, and such observations have been made by Unal & Rockwell (1988) who described it as an 'upstream wave motion'. Therefore, downstream disturbances may affect the upstream flow.

There is no established way of defining the near wake so here we define it as the region up to about ten diameters downstream from the cylinder; up to fifty diameters we have the intermediate wake, and beyond that we have the far or self-preserving wake (Matsumura & Antonia 1993). In the current work we subdivide the near wake into two regions: (*a*) the region just behind the cylinder up to three diameters downstream which is dominated by the dynamics of the shear layer – we will refer to it as the very near wake, and (*b*) the region between three and ten diameters, which we will refer to as simply the near wake.

There are still many unresolved fundamental issues regarding our understanding of the near wake. Some of these issues have been addressed for the far wake: for example, the question of coherent structures and flow organization has been addressed by Townsend (1979) who considered eddy structures in the far wake at $170D$ downstream, and by Hussain & Hayakawa (1987) who considered the region for $x/D \geqslant 10$ (D is the cylinder diameter and $x = 0$ is at the cylinder centre). Another fundamental question, considered by Matsumura & Antonia (1993) in the intermediate wake region, is how efficiently momentum is transported in the wake. However, the near wake is strongly three-dimensional, unlike the region downstream where quasi-one-dimensional assumptions may be used and point measurements may be sufficient. A third important issue relates to the question of existence of an inertial range and its extent as a function of Reynolds number in the subcritical regime, i.e. before the boundary layer becomes turbulent. From the modelling point of view, these questions are ultimately related to the dimensionality of the near wake, which measures the minimum number of degrees of freedom (or modes) required to effectively describe the dynamics of the near wake and thereby the dynamics of the vortex street downstream (Triantafyllou & Karniadakis 1990; Cao & Aubry 1993).

There are relatively few measurements available for the near wake owing to the special experimental arrangements required to obtain accurate data, as in the the experiments of Cantwell & Coles (1983) who provided measurements up to $x = 8D$ for Reynolds number $Re = 140\,000$. More recently, Lourenco & Shih (1994, see Beaudan & Moin 1994) have obtained mean and r.m.s. velocity profiles using PIV within the recirculation zone at $Re = 3900$. Also, streamwise and cross-flow velocity statistics were obtained in the near wake by Ong & Wallace (1996) at $Re = 3900$ using a multi-sensor hot-wire probe, but for $x/D \geqslant 3$. The aforementioned sensitivity of the very near wake to different experimental conditions is clearly reflected in the velocity measurements of such experiments. In figure 1 we plot the time-averaged centreline velocity at Reynolds number $Re = 3900$ from the experiments of Lourenco

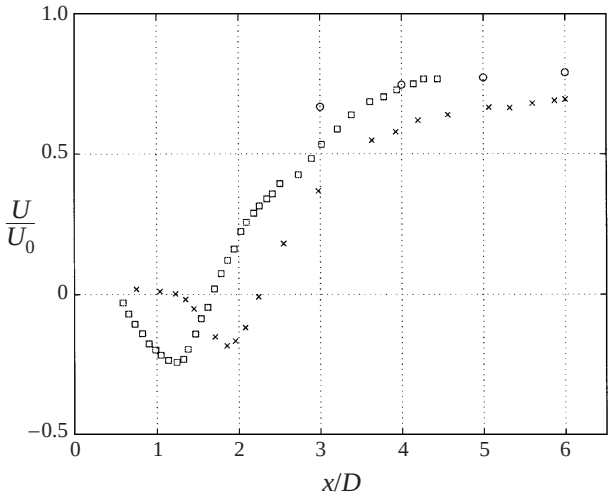

FIGURE 1. Experimental data: centreline velocity normalized by the free-stream velocity at $Re = 3900$. Squares are data of Lourenco & Shih, circles of Ong & Wallace, and crosses of Govardhan & Williamson.

& Shih and Ong & Wallace. We also include some more recent data of R. Govardhan & C. Williamson (private communications). The aspect ratio in the Lourenco & Shih experiment was 20.5 while in the Govardhan & Williamson experiments it was 10, which may explain the large difference in the formation length.† However, as it was pointed out by Noca, Park & Gharib (1998) in a recent systematic study, the formation length depends not only on the cylinder aspect ratio but on the cylinder diameter as well; the larger cylinder diameter could reduce the turbulence scales, stabilize the shear layers and thus lengthen the formation region. In the figure, we also see that the data of Ong & Wallace agree with the data of Lourenco & Shih for $x/D \geqslant 4$ but disagree at $x/d = 3D$. At present, it is not clear what other sources contribute to the discrepancy in these three experimental data sets.

As regards one-dimensional energy spectra of turbulent wakes behind circular cylinders, previous measurements were mostly for high Reynolds number flows and in the far wake. A systematic study of energy spectra 50–800 diameters downstream was presented in Uberoi & Freymuth (1969). It included a low Reynolds number range from about $Re = 300$ to 5000 and a higher one up to $Re = 95\,000$. It was clearly shown in that study that the inertial range in such flow regime depends strongly on the Reynolds number; for Reynolds number $Re \geqslant 1000$ at least a quarter of a wavenumber decade is present in the energy spectrum of the far wake. These results are in agreement with recent measurements reported in Marasli & Wallace (1993) at $Re = 2000$ for velocity and vorticity spectra obtained at 30 diameters ($x/D = 30$) downstream. More recently, streamwise and cross-flow velocity spectra were obtained in the near wake by Ong & Wallace (1996) at $Re = 3900$. Their data show that even in the near wake the velocity spectra have a similar form to the spectra measured in the far wake, and at this Reynolds number the inertial range extends to approximately half a decade in wavenumber.

Numerical simulation of turbulent wakes has been computationally prohibitive and only preliminary results have been obtained in Tomboulides, Orszag & Karniadakis

† Here we define the formation length based on the location of zero average velocity.

(1993) and Henderson & Karniadakis (1995) using direct numerical simulation (DNS). A more systematic study of the cylinder turbulent wake at $Re = 3900$ was undertaken by Beaudan & Moin (1994) who used large-eddy simulation (LES) with an upwind discretization. A second LES study was performed by Mittal & Moin (1996), with central differencing in order to control the numerical damping reported in the first study, and more recently a high-order LES study was completed by Kravchenko & Moin (1998). The results from the three studies are similar as far as the computed mean and r.m.s. velocities are concerned, i.e. LES predicts relatively accurately, although not uniformly, the experimental results in the region downstream of $x/D \geqslant 3$. However, in the very near wake all simulations converge to a mean velocity profile of U-shape (see figure 5; $x/D = 1.06$, dashed line) unlike the experiments of Lourenco & Shih that show a V-shape (see figure 5; $x/D = 1.06$, solid line). In contrast, an independent LES study by Rodi and co-workers (Frohlich *et al.* 1998) produced a V-shape velocity profile. Also, despite the higher fluctuations sustained in the central-differencing simulations by Mittal (1996), no clear inertial range was obtained in either of the first two LES studies, in contrast with the experiments. It is interesting to note that corresponding simulations with the subfilter model turned off produced a velocity spectrum almost identical to the LES. A systematic grid-refinement study performed in Beaudan & Moin (1994) also suggests that these results are resolution independent for at least the first ten diameters in the near wake. The high-order LES of Kravchenko & Moin, however, reproduced accurately the inertial range but predicted the same mean velocity field (i.e. U-shape) as the previous two simulations.

1.2. *Objectives*

As the use of the eddy-viscosity-based subfilter models and corresponding LES of such non-equilibrium flow may be questionable (Liu & Liu 1997), we have pursued both direct and large-eddy numerical simulation in our studies. The study of Moin and collaborators clearly shows that there is a stronger dependence of the results on the discretization scheme than on the subfilter model employed. Given these numerical uncertainties and the conflicting experimental results, we have decided to perform very systematic DNS and LES for this flow based on spectral discretizations. In particular, we have employed a numerical discretization based on a new class of hierarchical spectral methods on unstructured grids (Karniadakis & Sherwin 1999). They allow great flexibility in the discretization and dynamic refinement in modal space without the costly overhead associated with re-meshing. In Ma & Karniadakis (1997) we reported first results on comparisons between our DNS and LES of Beaudan & Moin (1994) and Mittal & Moin (1996). In the current study we have performed new and very detailed spectral DNS and LES from very low resolution using 200 000 degrees of freedom to very high resolution using 100 000 000 degrees of freedom.

The specific physical questions raised in the current work are:

What is the correct dynamics of the shear layer and how does it affect the very near wake, i.e. differences between the U-shape and V-shape mean velocity states?

What is the effect of an eddy-viscosity subfilter model on the flow properties?

Is there an inertial range in the turbulent near wake at low Reynolds number, and how close is the energy spectrum obtained from the spectral simulation to that of the experiment?

What is the contribution of the coherent motion to the mean flow and the Reynolds stresses?

How accurately are low-order statistics predicted, if the simulation cannot reproduce the spectrum of the physical laboratory?

Case	K	P	M	$L_z/(\pi D)$	c_s	C_p	St	Bubble length/D	Solution type
I	902	10	128	2.0	0.0	0.96	0.203	1.12	V-type
II	902	10	64	1.0	0.0	0.84	0.219	1.59	U-type
III	902	8	32	1.5	0.0	1.04	0.206	1.00	V-type
IV	902	8	32	1.5	0.032	0.898	0.213	1.28	V-type
V	902	8	32	1.5	0.196	0.765	0.208	1.76	U-type

TABLE 1. Summary of simulations. More cases for refinement studies are described in Appendix A.

What is the spatial structure of the most energetic modes and what is the dimensionality of the near wake?

To address these questions we have performed simulations of the flow past a circular cylinder at $Re = 500$, 1000, 3900 and 5000. The majority of the results presented here are for $Re = 3900$ for which we have experimental data available in the near wake for mean and r.m.s. velocities as well as spectra. We have implemented a modification to the phase-averaging technique used in the experimental study of Matsumura & Antonia (1993) in order to quantify the contribution of the organized motion to the average momentum transport. We have also developed a decomposition procedure based on the method of empirical eigenfunctions (Sirovich 1987) in order to also quantify the dimensionality of the near wake.

In the following, we briefly summarize the simulation approach and include validation details in the Appendices. We then present velocity statistics and comparisons with the experiments from the high-resolution simulation. Subsequently, we present the results of a very low-resolution simulation, which, surprisingly, are in good agreement with the experimental results. In the following section we discuss the spectrum of the near wake and compare with experimental and LES results. We then analyse this finding using phase averaging and a proper orthogonal decomposition of the fields at $Re = 3900$. We conclude with a summary and discussion.

2. Simulation parameters

2.1. *Unstructured grids and h and p refinement*

We performed direct and large-eddy numerical simulations using spectral/hp methods implemented in the incompressible Navier–Stokes solver $\mathcal{N}\epsilon\kappa\mathcal{T}\alpha r$ (Karniadakis & Sherwin 1999; Warburton 1998; Sherwin & Karniadakis 1995, 1996). This code is based on a new class of spectral algorithms on unstructured grids consisting of arbitrary triangulizations for dynamic remeshing; a Fourier expansion was employed along the homogeneous direction (cylinder-axis) with appropriate de-aliasing. Specifically, triangular elements are used, filled with Jacobi polynomial modes of order P corresponding to high-order mixed weights. The expansions are constructed so that they retain the tensor-product property (and thus the efficiency) of spectral methods. Unlike previous spectral element formulations which employed *nodal* expansions (Chu & Karniadakis 1993), the new expansions are *modal* and the only nodes needed are the vertices of the triangles. Moreover, the polynomial order can vary from element to element, readily accommodating p-type refinement. For wake flows, regions of intense vorticity can be captured and resolved dynamically using p-refinement.

We performed several simulations corresponding to h-refinement (i.e. with respect to number of elements K) and p-refinement (with respect to polynomial order P).

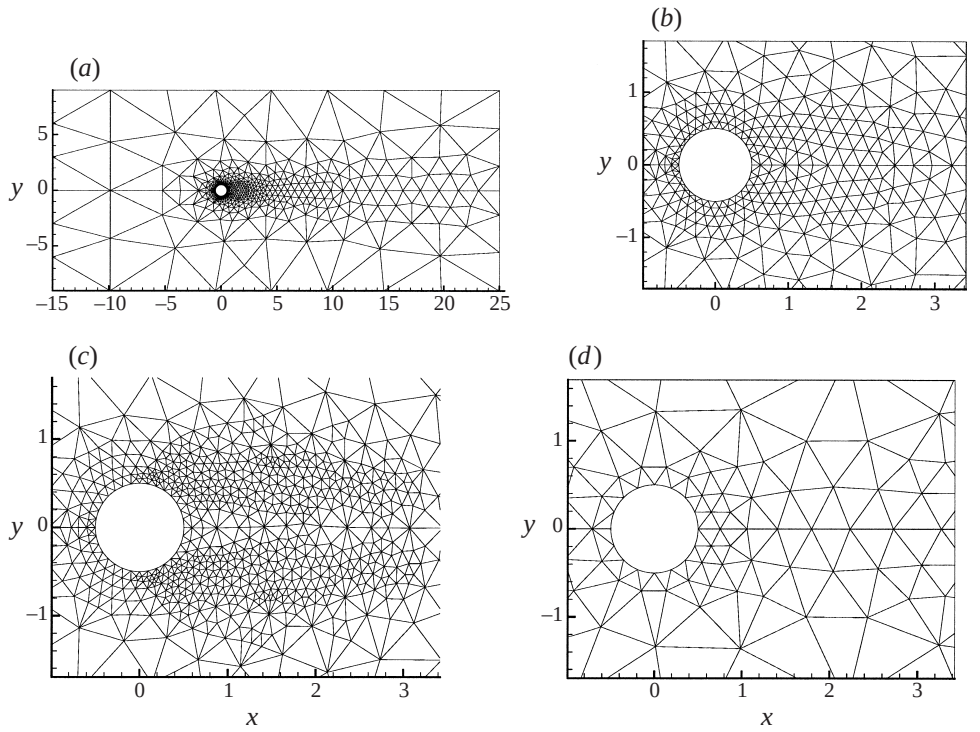

FIGURE 2. Two-dimensional 'z-slice' of the entire domain (a) and detail around the cylinder of the standard mesh ($K = 902$ elements, b); refined ($K = 1622$ elements, c); and coarse mesh ($K = 412$ elements, d) used in the $\mathcal{N}\epsilon\kappa\mathcal{T}\alpha r$ simulations. The unstructured grid shown is the skeleton based on which hierarchical spectral expansions are constructed.

A summary of the high-resolution DNS and LES runs is presented in table 1; more cases are shown in table 3 (Appendix A). In figure 2 we show a 'z-slice' of the computational domain in the (x, y)-plane with three different discretizations. Figure 2(b) shows a grid with $K = 902$ triangular prisms (elements), which has been the standard grid we have used for most cases. We also show a grid with finer resolution around the shear layers corresponding to $K = 1622$ elements (figure 2c), and also a grid with coarser resolution corresponding to $K = 412$ elements (figure 2d). The polynomial order per element varied from $P = 4$ to 10, and the number of Fourier modes varied from $M = 2$ to 128 (the corresponding number of physical points is twice the number of modes). Convergence in this method is obtained by either h- or p-refinement, the latter being faster than the former. A summary of the results from the resolution study is included in Appendix A. The finest resolution simulation employed $K = 902$ elements of order $P = 10$ and 256 points ($M = 128$ Fourier modes) in the spanwise direction. The lowest resolution employed $K = 412$ elements with $P = 6$ and only $M = 2$, i.e. a severe truncation of Fourier modes in the spanwise direction.

2.2. *Computational domain*

The domain extends from $-15D$ at the inflow to $25D$ at the outflow, and from $-9D$ to $9D$ in the cross-flow direction. Neumann boundary conditions (i.e. zero flux) were used at the outflow and on the sides of the domain to minimize the effect of normal boundary layers at the truncated domain. The spanwise length was varied

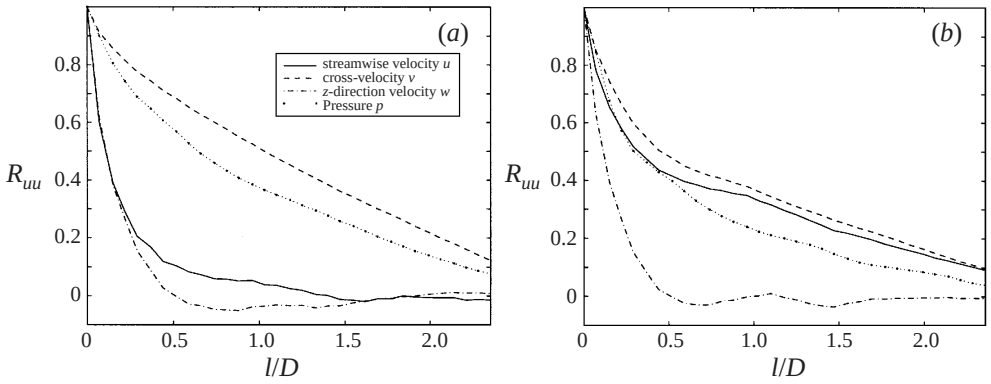

FIGURE 3. Autocorrelation function for the three velocity components and pressure. (*a*) Centreline point; (*b*) off-centreline point. ($Re = 3900; L_z/D = 1.5\pi$.)

as $L_z/D = \pi/2, \pi, 1.5\pi, 2\pi$. For reference, the spanwise length used in all simulations of Beaudan & Moin (1994), Mittal & Moin (1996) and Kravchenko & Moin (1998) was $L_z/D = \pi$. The experimental results of Ong & Wallace (1996) suggest a value of correlation length less than $1.5D$ at three diameters downstream; this was obtained using the streamwise velocity only. Other meaurements by Mansy, Yang & Williams (1994) have shown a dependence of the correlation length of the form $20Re^{-0.5}D$, where $Re = U_0 D/\nu$ is the free-stream Reynolds number. This empirical formula, which was constructed using data in the range $300 \leqslant Re \leqslant 1200$, if extrapolated to $Re = 3900$ predicts a very low spanwise length of $0.32D$ at three diameters downstream. The experiment of Mansy *et al.* shows that this value increases to about $1D$ for $x/D \geqslant 10$. This discrepancy in length scales seem to correspond to two distinct spanwise length scales associated with two different systems of streamwise vortices, as documented by Williamson, Wu & Sheridan (1995).

The definition of the correlation length in Mansy *et al.* (1994) is different from the standard definition used in most experimental studies and was based on instantaneous autocorrelation functions. Specifically, the location of the first maximum of the oscillatory autocorrelation function was taken as the spanwise correlation length. Here, we have also computed the correlation length based on the autocorrelation function of each velocity component but defined as in the experimental studies of Ramberg & Griffin (1976)

$$R_{uu}(l; x, y) = \frac{\overline{u'(x, y, z, t)u'(x, y, z - l, t)}}{\overline{u'^2(x, y, z, t)}}, \tag{2.1}$$

where the bar denotes averaging over time and over z-planes. Also, $u'(x, y, z, t)$ is the fluctuation obtained after we subtract the mean quantity, i.e. averaged in time and span (z) at the point (x, y). We have computed the correlation length based on equation (2.1) by both averaging in time or averaging in span first, and subsequently averaging in span or in time, respectively. For sufficient fine resolution in span and temporal sampling, as in our simulations, there is no difference in the results. We include in the plots the autocorrelation function for all three velocity components and the pressure. A typical result is shown in figure 3 for $L_z/D = 1.5\pi$ where we see that at a centreline point R_{uu} drops to zero at about $1.5D$ but that, in general, at points off-centreline R_{vv} and R_{uu} do not decay as fast. In figure 4 we plot the autocorrelation function for the larger span $L_z/D = 2\pi$ corresponding to the highest resolution DNS

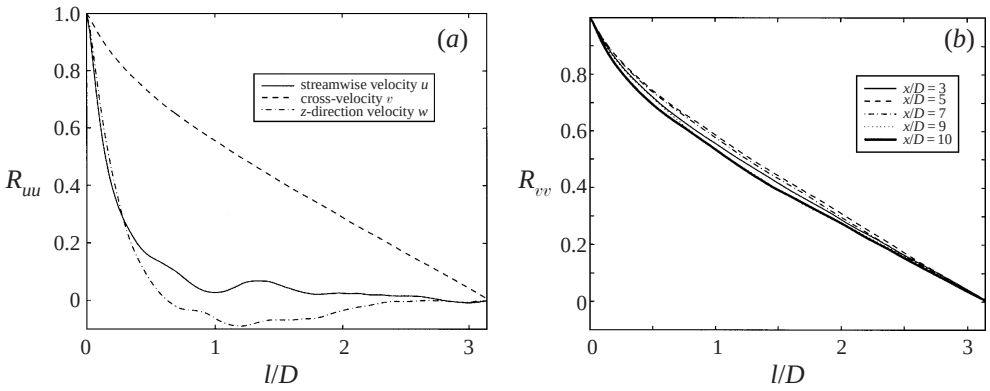

FIGURE 4. Autocorrelation function at the centreline: (*a*) three velocity components at $x/D = 3$; (*b*) Cross-flow velocity at different $x/D = 3, 5, 7, 9, 10$ locations. ($Re = 3900$; $L_z/D = 2\pi$.)

we performed in this work (Case I). We see that in the larger domain the correlation is in general higher, especially in the cross-flow component.

These results indicate that values of R_{uu} obtained in experiments at centreline points may underpredict the spanwise correlation length. Therefore, it may be inadequate to use R_{uu} as the only criterion in deciding on the domain size. Indeed, we will see in the following that the span length is very important in determining the r.m.s. values in the very near wake and correspondingly the mean velocity profiles. In general, our results at $Re = 3900$ are consistent with computed results at $Re = 1000$ where the spanwise correlation length is about $6D$ (Evangelinos 1999). They are also consistent with experimental results by Ramberg & Griffin (1976), regarding the trend of the value of correlation length as function of Reynolds number. They have measured a correlation length of about $10D$ in the Reynolds number range 500–600. Clearly, as the Reynolds number increases the spanwise correlation length decreases in this subcritical regime.

2.3. *Subfilter model*

The equations of motion for a large-eddy simulation are

$$\frac{\partial(\tilde{u}_i)}{\partial x_i} = 0, \quad \frac{\partial(\tilde{u}_i)}{\partial t} + \frac{\partial(\tilde{u}_i\tilde{u}_j)}{\partial x_j} = -\frac{\partial \tilde{p}}{\partial x_i} + \frac{\partial}{\partial x_i}\left\{(\nu + \nu_s)\left[\frac{\partial \tilde{u}_i}{\partial x_j} + \frac{\partial \tilde{u}_j}{\partial x_i}\right]\right\}, \tag{2.2}$$

where the term ν_s represents the Smagorinsky eddy-viscosity model, defined as $\nu_s = l_s^2|\tilde{S}|$, with $|\tilde{S}| = (2\tilde{S}_{ij}\tilde{S}_{ij})^{1/2}$ the magnitude of the filtered strain-rate tensor. Here, l_s is the *Smagorinsky length scale* or *subfilter length scale*. It is equal to $l_s = c_s\Delta$, where c_s is the *Smagorinsky constant,* and Δ is the filter width. In structured grids typically $\Delta = \left(\Delta_x\Delta_y\Delta_z\right)^{1/3}$, where $\Delta_x, \Delta_y, \Delta_z$ are the filter widths in each direction. For the spectral/*hp* element method on triangles, the filter width Δ has to be defined properly in order to account for the *sub-cell resolution*. Following the heuristic argument in Gottlieb & Orszag (1977), the polynomial order, P, and resolved half-wavenumber, k, are related by $P = k\pi$. A new definition of Δ is thus proposed, based on the area of the triangle, A, and the grid spacing, Δz, in the Fourier direction, of the form

$$\Delta = \left(A\left(\frac{\pi}{P}\right)^2\Delta z\right)^{1/3}. \tag{2.3}$$

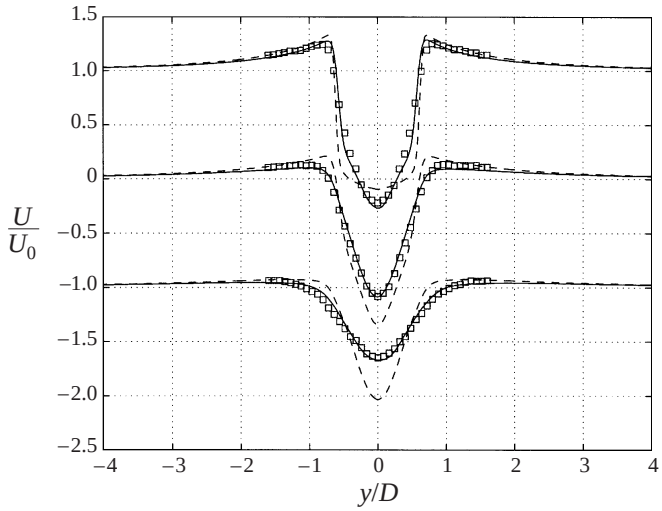

FIGURE 5. DNS mean streamwise velocity predictions at $x/D = 1.06$, 1.54, 2.02 (from top to bottom, respectively). Case I (wide domain – solid line) and Case II (narrow domain – dashed line). Squares are data of Lourenco & Shih.

Numerical experiments with decaying homogeneous turbulence and turbulent channel flow have justified this choice (see Karamanos 1999).

In the current work, we perform two LES for the standard grid of $K = 902$ elements at $Re = 3900$. The first case (Case IV) corresponds to $c_s = 0.032$, employed in the channel simulation of Moin & Kim (1982), and the second case (Case V) to $c_s = 0.196$, based on the value of Lilly's (1967) theory. These values have been adjusted from the classical values to take into account the sub-cell resolution employed in the spectral/*hp* element discretization. In the near-wall region, the Panton (1997) wall damping function is used which follows the correct y^3 behaviour.

3. High-resolution simulations

In this section we present results from the two highest resolution DNS runs, one with span length $L_z/D = 2\pi$ (Case I) and the other one with $L_z/D = \pi$ (Case II); see table 1. We also compare two LES runs (Cases IV, V) at a slightly lower resolution and a DNS run (Case III) at the same resolution. We will show that depending on the spanwise extent of the domain and the dissipation of the LES subfilter model, there exist two converged states which are distinctly different in the very near wake.

3.1. *The very near wake: U-shape versus V-shape*

We first present comparisons of DNS predictions with experimental data for $x/D \leqslant 3$ at $Re = 3900$. We concentrate on mean and r.m.s. streamwise velocity profiles. Similar PIV experimental data have been obtained by Lourenco & Shih and were published in Beaudan & Moin (1994); streamwise data are significantly more reliable than the cross-flow velocity measurements. For example, the experimental uncertainty in the measurements of the streamwise velocity is about 5% while for the cross-flow velocity is more than 50% according to Beaudan & Moin (1994). In figure 5 we see that very good agreement is obtained for Case I, unlike Case II. In particular, a pronounced feature of Case I is the V-shape velocity profile at $x/D = 1.06$ in contrast with the U-shape (flat) profile of Case II. However, as documented in Appendix A, both DNS

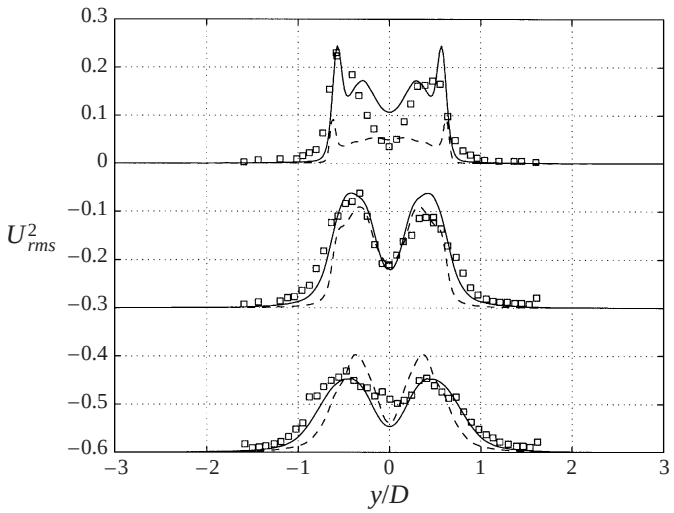

FIGURE 6. DNS r.m.s. streamwise velocity predictions at $x/D = 1.06$, 1.54, 2.02 (from top to bottom, respectively). Symbols as figure 5.

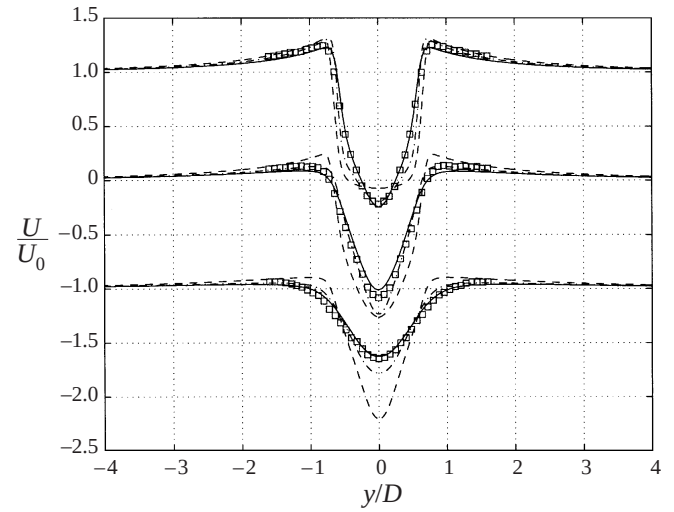

FIGURE 7. LES mean streamwise velocity predictions at $x/D = 1.06$, 1.54, 2.02. Case III (no subfilter – solid line), Case IV (low subfilter – dash-dot line), and Case V (high subfilter – dashed line). Squares are data of Lourenco & Shih.

predictions are converged solutions of the Navier–Stokes equations for Case I (wide domain) and Case II (narrow domain). In order to examine these quantitative and also qualitative differences, we plot in figure 6 the r.m.s. values of the streamwise velocity at the same locations. We see that at $x/D = 1.06$ the velocity fluctuations of Case I match the experimental values, which are at a much higher magnitude than those of Case II. The higher fluctuations lead to better flow mixing locally, which justifies the corresponding shape of the mean velocity profile. Also, at the other two locations the Case I predictions are in closer agreement with the experimental results than Case II.

Next we examine the predictions of two LES runs, one with a low value of the

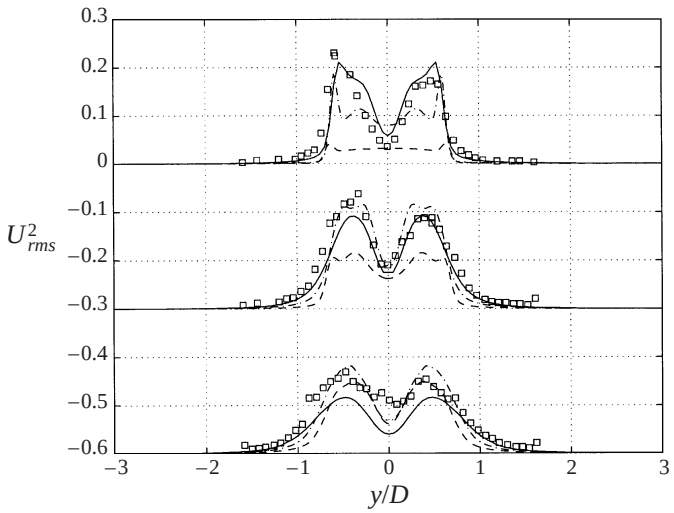

FIGURE 8. LES r.m.s. streamwise velocity predictions at $x/D = 1.06, 1.54, 2.02$. Symbols as figure 7.

Smagorinsky constant c_s (Case IV) and the other one with a high value of c_s (Case V). Case III represents a DNS run at the same resolution (i.e. no subfilter model). All three runs have exactly the same resolution; here the spanwise length was kept constant at $L_z/D = 1.5\pi$. We see in figure 7 that again both U-shape and V-shape mean flow states emerge. In particular, the stronger the subfilter model dissipation the flatter the profile, with a U-shape profile clearly obtained in Case V. In contrast, a V-shape profile is obtained with the model off. The predictions of low-dissipation LES (Case IV) resemble more closely the DNS and the experimental results. The predictions for the r.m.s. values are also consistent with these mean velocities profiles as shown in figure 8. The U-shape profile corresponds to small fluctuations in the near wake, and overall the low-coefficient LES (Case IV) is closer to the V-shape state.

The systematic LES of Moin and collaborators (Beaudan & Moin 1994; Mittal & Moin 1997; Kravchenko & Moin 1998) are for span $L_z/D = \pi$ and they all converge to a U-shape profile. Another LES study for the same conditions has been performed by Frohlich *et al.* but only partial results have been published in Frohlich *et al.* (1998). They have used both a structured and an unstructured grid. In figure 9 we plot again the experimental results with DNS (Case I) and the aforementioned LES. We also include our results from a very low-resolution DNS (see § 4). We see that the high-resolution DNS as well as the structured mesh LES (with the standard Smagorinsky model) of Frohlich *et al.* agree with the experimental data. In contrast, the dynamic Smagorinsky model of Beaudan & Moin predict a large velocity defect at this location whereas the low-resolution DNS as well as the unstructured mesh LES of Frohlich *et al.* predict a smaller velocity defect at this location. The asymmetry in the profile obtained from the unstructured mesh LES of Frohlich *et al.* is probably due to insufficient time averaging. The structured LES of Frohlich *et al.* was performed with a large number of points corresponding to $166 \times 166 \times 48$ points in the radial, azimuthial, and spanwise directions, respectively, higher than the simulation of Beudan & Moin ($116 \times 136 \times 48$) but lower than the simulation of Mittal & Moin ($401 \times 120 \times 48$).

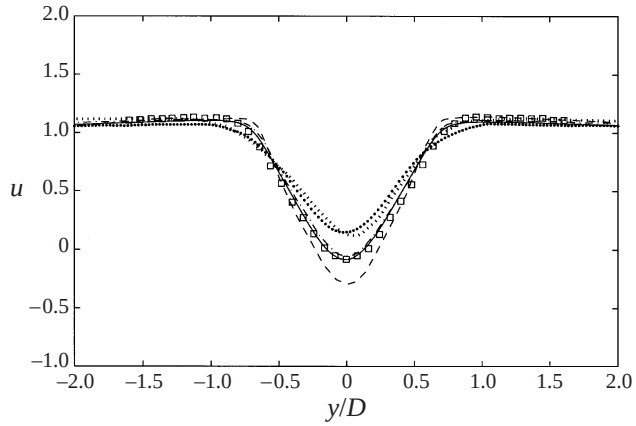

FIGURE 9. Streamwise mean velocity profile at $x/D = 1.54$. Squares denote experimental data of Lourenco & Shih, solid line DNS (Case I) high-resolution, dark dots DNS low-resolution, dashed line dynamic model of Beaudan & Moin, dash-dot line structured mesh/Smagorinsky of Frohlich *et al.*, and light dots unstructured mesh/Smagorinsky of Frohlich *et al.*

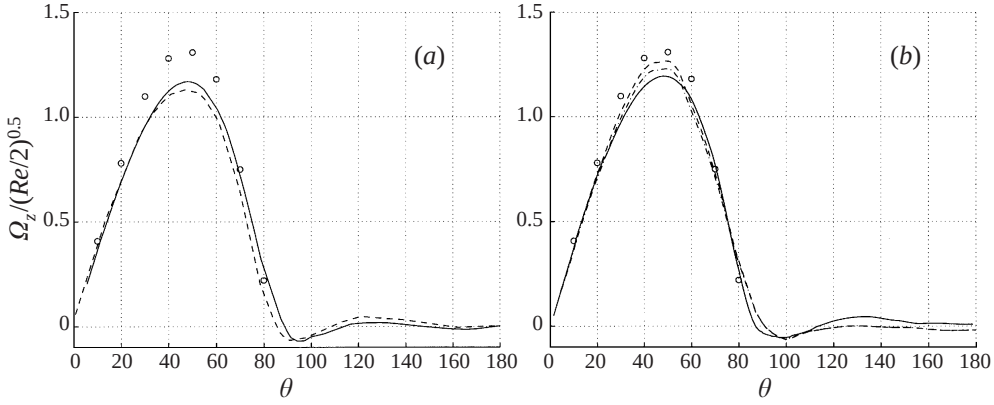

FIGURE 10. Time-averaged vorticity distribution on the cylinder surface at $Re = 3900$. Circles denote experimental data of Son & Hanratty at $Re = 5000$. (*a*) DNS comparison for Case I (solid line) and Case II (dashed line). (*b*) LES comparison for Case III (solid line), Case IV (dash-dot line), and Case V (dashed line).

3.2. *Cylinder surface*

The two different mean states in the very near wake correspond to different sizes of the mean separation region as shown in table 1, with the U-shape profile corresponding to a longer formation length than the V-shape. These two distinct solutions also correspond to different distributions of the average vorticity on the cylinder surface as well as the pressure coefficient.

In figure 10 we plot the mean spanwise vorticity (averaged in the span and in time) along with experimental data obtained by Son & Hanratty (1969) at $Re = 5000$. We non-dimensionalize with the factor $\frac{1}{2}\sqrt{Re}$, consistent with the boundary layer theory for the non-separated part of the flow. Both DNS and LES underpredict the experimental data which were obtained using electrochemical techniques. Note that the bounday layer predictions are also below the experimental data, as documented by Son & Hanratty (see their figure 15). Results from a two-dimensional simulation

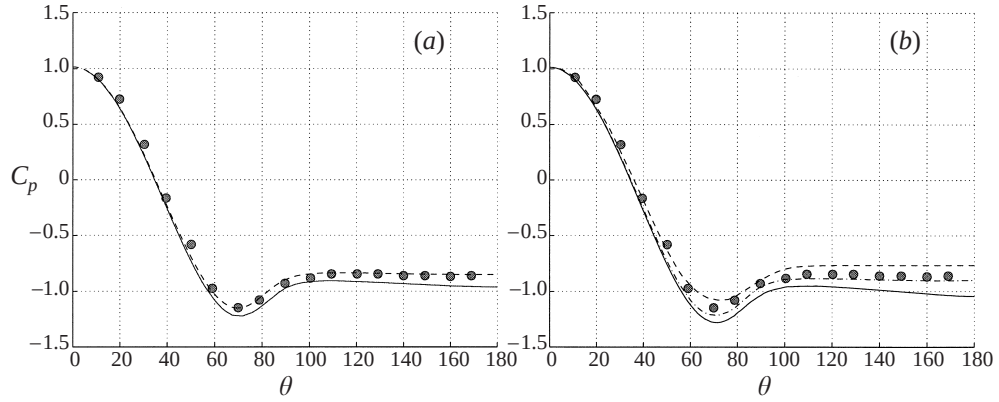

FIGURE 11. Time-averaged pressure coefficient distribution on the cylinder surface at $Re = 3900$. Circles denote experimental data of Norberg (1987) at $Re = 3000$. (*a*) DNS comparison for Case I (solid line) and Case II (dashed line). (*b*) LES comparison for Case III (solid line), Case IV (dash-dot line), and Case V (dashed line).

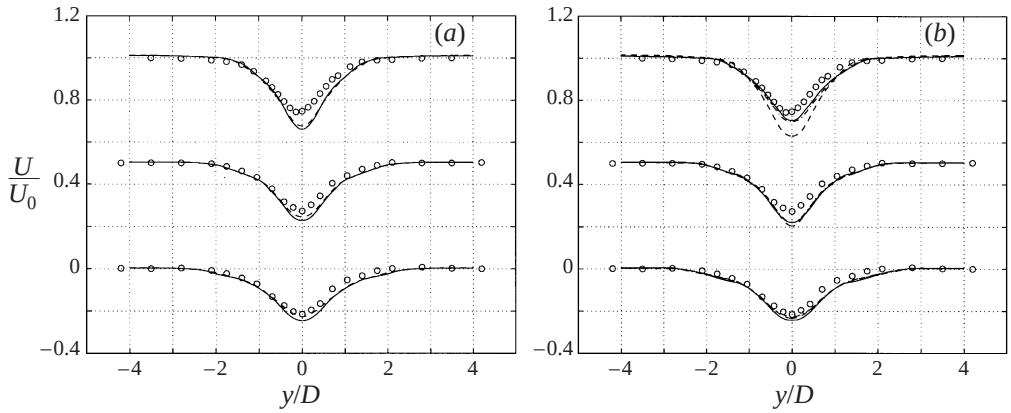

FIGURE 12. Mean streamwise velocity profiles at $x/D = 4$, 7, 10 (from top to bottom, respectively). Circles denote experimental data of Ong & Wallace at $Re = 3900$. (*a*) DNS comparison for Case I (solid line) and Case II (dashed line). (*b*) LES comparison for Case III (solid line), Case IV (dash-dot line), and Case V (dashed line).

Ma (2000) reveal a similar distribution except in the wake region, where a much smaller separation bubble is obtained than in the three-dimensional simulation. In figure 11 we plot the pressure coefficient from the DNS and LES predictions along with the experimental data of Norberg (1994) at $Re = 3000$. We see that the DNS U-shape solution (Case II) is closer to the experimental results than all other cases; the sensitivity of the base pressure coefficient to various conditions has been studied systematically by Norberg who showed a very significant variation depending on the aspect ratio of the cylinder in this range of Reynolds number.

3.3. *Statistics for* $x/D \geqslant 3$

To evaluate the accuracy of DNS and LES in the region downstream we use the experimental data of Ong & Wallace (1996) who obtained mean velocities and turbulence intensities at locations $x/D \geqslant 3$. In figure 12 we plot mean velocity profiles at $x/D = 4, 7$ and 10 and we see that the comparison is also good for all predictions.

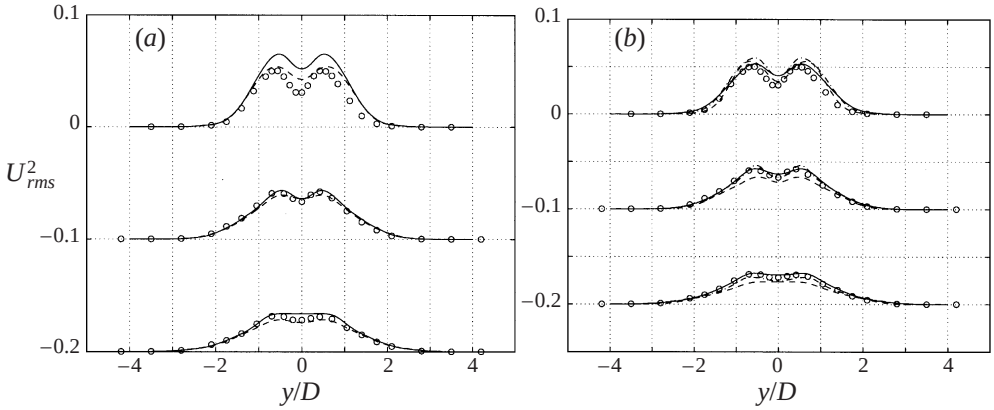

FIGURE 13. Root-mean-square streamwise velocity profiles at $x/D = 4$, 7, 10. Circles denote experimental data of Ong & Wallace at $Re = 3900$. (*a*) DNS comparison for Case I (solid line) and Case II (dashed line). (*b*) LES comparison for Case III (solid line), Case IV (dash-dot line), and Case V (dashed line).

The same is true for the r.m.s. values as shown in figure 13 and also for the cross-flow velocity as shown in Appendix B. These results show that the region beyond $x/D \geqslant 3$, which is dominated by the vortex shedding is less sensitive to the aforementioned factors, unlike the very near wake which is very sensitive to turbulence intensity. In this flow, turbulence fluctuations are influenced primarily by the background noise and the cylinder aspect ratio.

4. Low-resolution simulations

We examine next how the results presented in § 3 are affected by substantially reducing the grid resolution and without using any subfilter model. In particular, we will present here results obtained on the grids shown in figure 2(*d*) consisting of $K = 412$ triangular elements and only $P = 6$ and the equivalent $K = 902$ and $P = 4$, both cases corresponding to approximately the same number of degrees of freedom. More comparisons with the subfilter model on the same grid can be found in Karamanos (1999). We will first use only two Fourier modes in the span, i.e. the mean mode and one perturbation ($M = 2$ or four points). We also choose a small value for the spanwise length $L_z/D = \pi/2$.

A similar effort was undertaken in the work of Zores (1989) for simulating turbulent flow in a channel. He showed that even severely truncated spectral expansions (corresponding to resolution of $4 \times 4 \times 16$) give very good predictions of the mean velocities and less so for the turbulence intensities, though still comparable to LES results of Moin & Kim (1982). For the low-resolution simulations, it is important to integrate for a very long time to obtain reasonable results. This was found in the study of Zores (1989) and confirmed here in our study; the results we present next have been integrated for at least 100 shedding cycles.

We compare first with the experiments of Lourenco & Shih in the very near wake and subsequently with the experiments of Ong & Wallace farther downstream. In figure 14 we plot the mean streamwise velocity profile at locations $x/D = 1.06, 1.54$ and 2.02. We also include the experimental data of Lourenco & Shih taken from Beaudan & Moin (1994), and the LES data of Beaudan & Moin. We see that the predictions from both low-resolution simulations without subfiltering are comparable

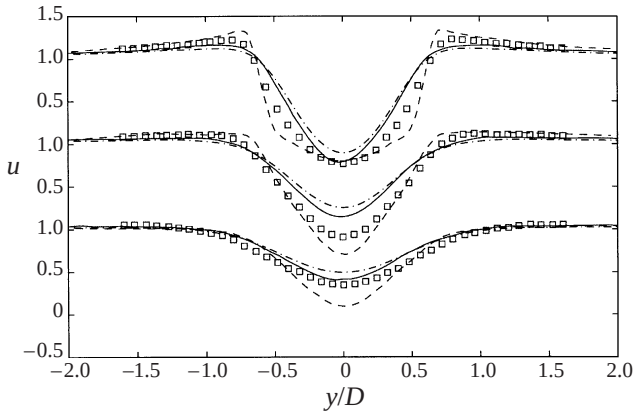

FIGURE 14. Streamwise mean velocity profile at $x/D = 1.06$, 1.54, 2.02 (top to bottom). Squares denote experimental data of Lourenco & Shih, solid line DNS ($K = 412$, $P = 6$), dash-dot line DNS ($K = 902$, $P = 4$) and dashed line LES of Beaudan & Moin.

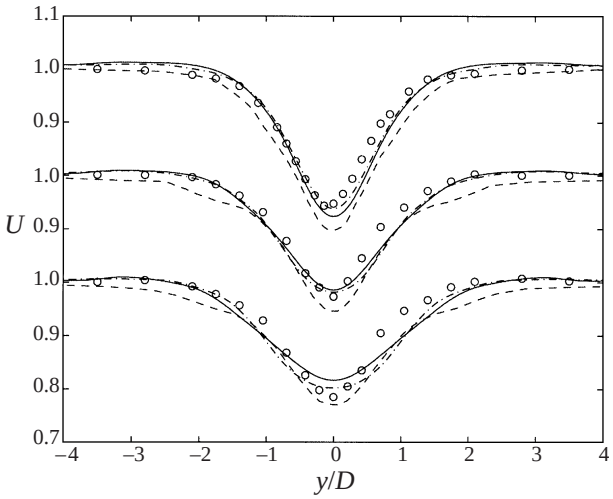

FIGURE 15. Mean velocity profiles at $x/D = 4$, 7, 10 (top to bottom). Circles denote experimental data of Ong & Wallace, solid line DNS ($K = 412$, $P = 6$), dash-dot line DNS ($K = 902$, $P = 4$) and dashed line LES of Beaudan & Moin.

to the LES predictions. In figures 15, 16 we plot the mean streamwise velocity and turbulent fluctuations, respectively, at locations $x/D = 4$, 7, 10 and compare with the experimental data of Ong & Wallace. The predictions for the mean velocities are good but the streamwise turbulence intensity shows some wiggles, which is an indication of insufficient resolution. However, the low-resolution spectral simulations obtain an overall better agreement with the experimental data than the dissipative LES predictions reported in Beaudan & Moin (1994).

The results presented so far were obtained with only $M = 2$ Fourier modes employed along the cylinder span. Of interest is to examine the influence of the number of Fourier modes M on the mean velocity profiles presented above while retaining the same resolution in the (x, y)-planes. We performed additional simulations with $M = 8$ and 32 and also a two-dimensional simulation. As we see in figure 17 there is essentially no difference in the predicted mean streamwise velocity profile from

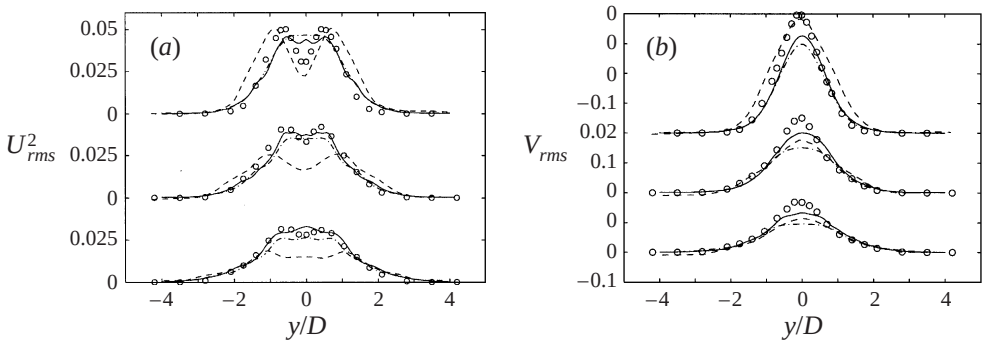

FIGURE 16. (*a*) Turbulent intensity of the streamwise velocity ($u^2_{\mathrm{r.m.s.}}$) at $x/D = 4$, 7, 10. (*b*) Turbulent intensity of the cross-flow velocity ($v^2_{\mathrm{r.m.s.}}$) at $x/D = 4$, 7, 10. Circles denote experimental data of Ong & Wallace, solid line DNS ($K = 412$, $P = 6$), dash-dot line DNS ($K = 902$, $P = 4$) and dashed line LES of Beaudan & Moin.

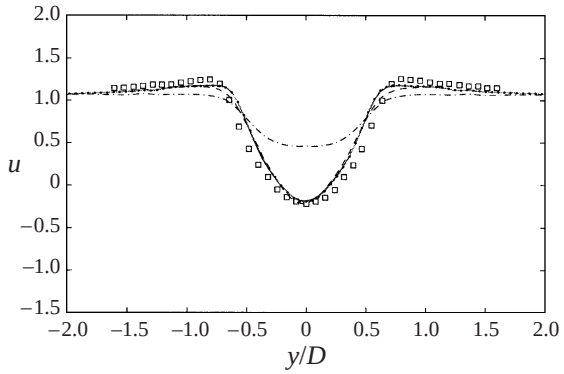

FIGURE 17. Streamwise mean velocity profile at $x/D = 1.06$ for different Fourier modes employed along the span. Squares denote experimental data of Lourenco & Shih, dash-dot line 2D simulation, dashed line $M = 2$, dot-solid line $M = 8$ and solid line $M = 32$ (coincides with $M = 8$).

$M = 2$ to $M = 32$ but the two-dimensional prediction deviates substantially. The cases with $M = 8$ and $M = 32$ correspond to almost identical predictions suggesting convergence in the z-direction. The $M = 2$ case is closer to the questionable (for the cross-flow component) experimental results, as shown in Appendix B.

The results presented in this section indicate that the first Fourier mode ($M = 1$) carries most of the spanwise energy for the chosen span $L_z/D = \pi/2$, as it is evident by comparing with the two-dimensional results in figure 17. This has been independently verified by computing the averaged plane-modal energy $E_{xy}(m) = \int_{xy}[u_m^2 + v_m^2 + w_m^2]\,\mathrm{d}x\,\mathrm{d}y$ and observe its decay with respect to the mode number Ma (2000).

Given the surprisingly good results with this low resolution at $Re = 3900$, we performed another set of simulations with the same low resolution and with only $M = 2$ Fourier modes at $Re = 5000$ for which we had available experimental data from the work of Zhou & Antonia (1993). In figure 18 we plot the mean velocity profile and the streamwise turbulent intensity $\overline{u'^2}$ at station $x/D = 10$. Again, we see that despite some wiggles in the numerical results the agreement with the experimental results is good.

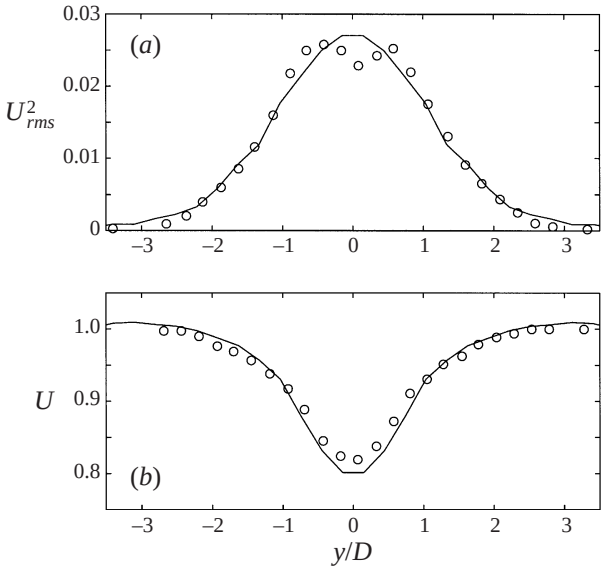

FIGURE 18. Streamwise mean velocity profile (b) and turbulent fluctuation (a) at $x/D = 10$ and $Re = 5000$. The experimental data (circles) are from Zhou & Antonia (1993).

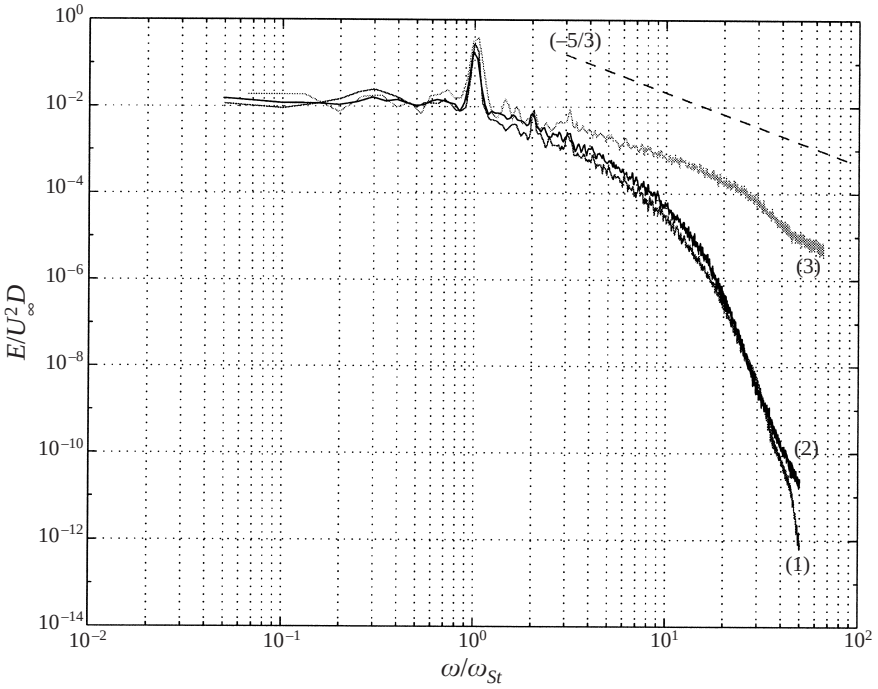

FIGURE 19. One-dimensional streamwise velocity spectrum (energy versus normalized frequency) in the near wake of flow past a cylinder at $Re = 500$ (curve 1), 1000 (curve 2), and 3900 (curve 3).

5. The spectrum of the near wake

We now turn to the question of the extent of inertial range in this relatively low Reynolds number regime. First, we plot in figure 19 spectra from our DNS at $Re = 500$, 1000 and 3900. The standard non-dimensionalization with the free-stream

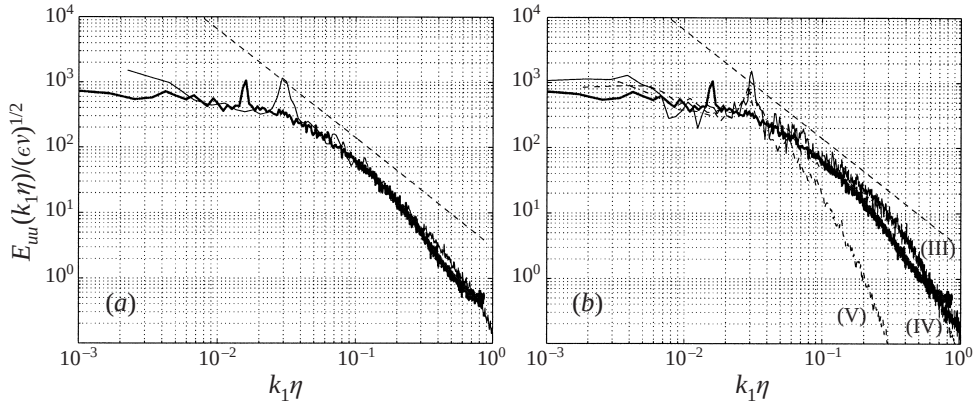

FIGURE 20. Streamwise velocity spectrum at the centreline point $x/D = 3.0$ and $Re = 3900$. (*a*) DNS (Case I – thin line) versus experiment of Ong & Wallace (thick line); (*b*) LES (Case IV, low subfilter), (Case V, high subfilter) and (Case III, no subfilter). The dashed line indicates the $-\frac{5}{3}$ slope.

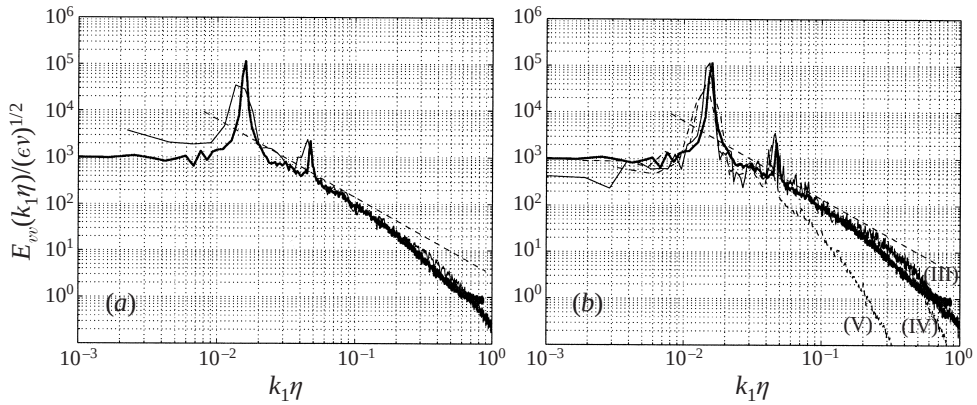

FIGURE 21. As figure 20 but for cross-flow velocity spectrum.

velocity and the cylinder diameter is used here. The point recorded for $Re = 500$ and 1000 is at ($x/D = 3$, $y/D = 1$) and at ($x/D = 2.57$, $y/D = 0.52$) for $Re = 3900$. We see that a substantial inertial range exists only for the $Re = 3900$ flow.

In figure 20 we plot the one-dimensional k_1 wavenumber spectrum of the streamwise velocity at $x/D = 3$ (centreline) normalized with Kolmogorov scaling at $Re = 3900$ and compare DNS and LES with experimental results. On figure 20(*a*) we include data from the high-resolution simulation with the wide domain (Case I) and the experimental data of Ong & Wallace, and on figure 20(*b*) we plot our two LES runs (Cases IV, V) against the same experimental data, and the corresponding DNS (Case III, subfilter model off). This is a frequency spectrum converted to wavenumber spectrum with the use of Taylor's hypothesis following Ong & Wallace (1996). Note that the experimental data erroneously show a peak at the Strouhal frequency, which is evidence that the spectrum was not measured exactly at the centreline. Due to symmetry conditions only a pronounced peak at twice the Strouhal frequency should be present at the centreline. Overall, very good agreement is obtained with the experiment for all cases except the LES Case V corresponding to strong subfiltering. The effect of excessive dissipation leads to fast decay and thus the inertial range is

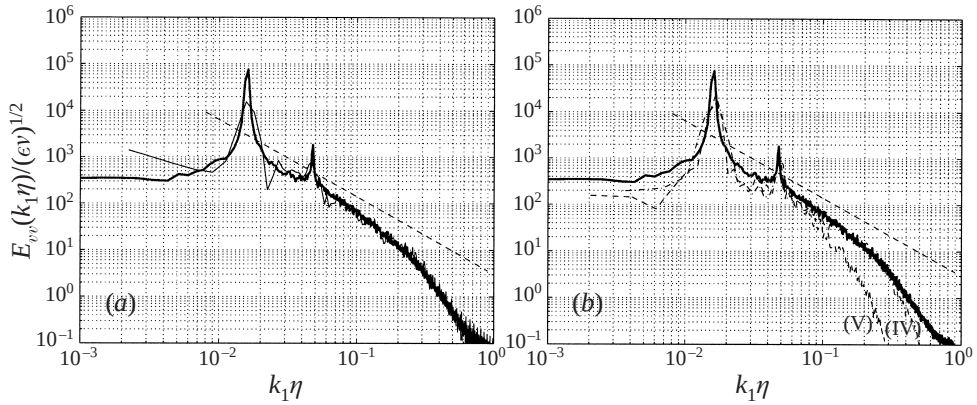

FIGURE 22. As figure 21 but at the centreline point $x/D = 7.0$.

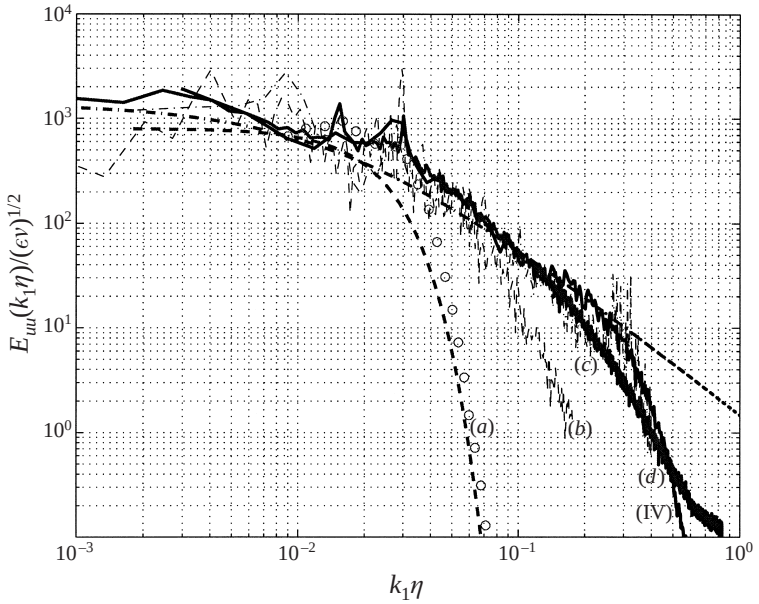

FIGURE 23. One-dimensional streamwise velocity spectrum (Kolmogorov scaling) at the centreline point $x/D = 5$. (*a*) Beaudan & Moin; (*b*) Mittal & Moin. (*c*) Kravchenko & Moin. (*d*) experiment Ong & Wallace; (IV) spectral LES, Case IV; the dashed lines are explained in figure 24. The LES spectrum (*c*) oscillates above a cutoff wavenumber unlike the spectral LES (Case IV).

not captured. All other results confirm that an inertial range exists in the very near wake. This is also evident in the spectra of the cross-flow velocity at the same location as shown in figure 21. The same picture emerges in all other locations downstream, where spectra have been obtained. We plot in figure 22 spectra of the cross-flow velocity at $x/D = 7$ which again show very good agreement with the experiment except the over-dissipative LES case (Case V). Note that the Strouhal peaks are predicted correctly in the cross-flow spectra.

Next, we compare results of our spectral LES with other published LES predictions. In figure 23 we plot the one-dimensional k_1 wavenumber spectrum of the streamwise velocity normalized with Kolmogorov scaling at a centreline point $x/D = 5$. It is

clear that the LES studies of Beaudan & Moin (1994) and Mittal & Moin (1997) do not predict accurately the inertial range, in accord with our high-c_s LES run (Case V). However, the high-order LES of Kravchenko & Moin agrees very well with the experiment and with our LES (case IV) up to the point where there is an onset of high-frequency fluctuations due to the grid size limitation. Also, at low frequencies there are some oscillations which are due to relatively short time averaging. For example, the length of the time record of Beaudan & Moin (1994) was 30 convective units or equivalently approximately 6 shedding cycles and it was enhanced by forming an average over 48 records at different points in the homogeneous (cylinder-axis) direction. The low-pass filter cut-off frequency in the experiments was at $k_1\eta \approx 0.7$, which may explain the upwards direction of the high-wavenumber end of the spectrum. Also shown in the plot is a curve that describes von Kármán's interpolation formula to connect the inertial subrange with the low-wavenumber end of the spectrum

$$E_u/(\epsilon\nu)^{1/2}\eta = A(1 + Bk_1\eta)^{-5/3}, \tag{5.1}$$

which usually applies to high Reynolds number, with A, B empirical constants and η the Kolmogorov length scale. In addition, we included the low Reynolds number limit for the spectrum which has the form

$$E_u/(\epsilon\nu)^{1/2}\eta = A^* \exp(-\pi(Ck_1\eta)^2/4), \tag{5.2}$$

where A^*, C are empirical constants. More specifically, this form corresponds to the limit where the inertial terms can be neglected in isotropic turbulence. It is shown in figure 23 that appropriate constants A^* and C can be chosen so that this curve fits the spectrum obtained by Beaudan & Moin. The fact that this spectrum (equation (5.2)) corresponds to the zero Reynolds number limit is consistent with the findings of Beaudan & Moin that excessive numerical dissipation in their simulation damps small-scale turbulence. The results of Mittal & Moin (1997) obtained with significantly higher resolution are somewhat improved (curve (6) in figure 24). Also, both our spectral LES and the high-order LES of Kravchenko & Moin predict accurately the inertial range (see figure 23).

The energy spectra presented so far were obtained from the high-resolution simulation. The low-resolution simulation with only $M = 2$ modes predicts an erroneous spectrum, but we wanted to examine what happens as we increase the number of modes in the spanwise direction to $M = 8$ and $M = 32$. The results for these two cases are similar, and here we present in figure 24 the one-dimensional k_1 wavenumber spectrum of the streamwise velocity for the case $M = 8$. This is a frequency spectrum recorded at the point ($x/D = 2.55$, $y/D = 0.45$) and converted to wavenumber spectrum with the use of Taylor's hypothesis as before. The time series extends over 624.89 convective time units (tD/U_∞), which is approximately 131 shedding cycles. This corresponds to two runs, the first run for 300.25 convective units with a time step $\Delta t = 0.002$ and with velocity history recorded every 10 time steps, and the second run with $\Delta t = 0.003$ and velocity data recorded every 20 time steps. No other processing of the data was used except pre-processing with a Hanning window to correct for end effects. As seen in figure 24, the low-resolution spectral simulation is in agreement with the experimental results including the inertial range.

6. Low-dimensionality in the wake

The results so far have shown that while the shear layer in the very near wake ($x/D < 3$) is sensitive to resolution and aspect ratio, the region downstream which

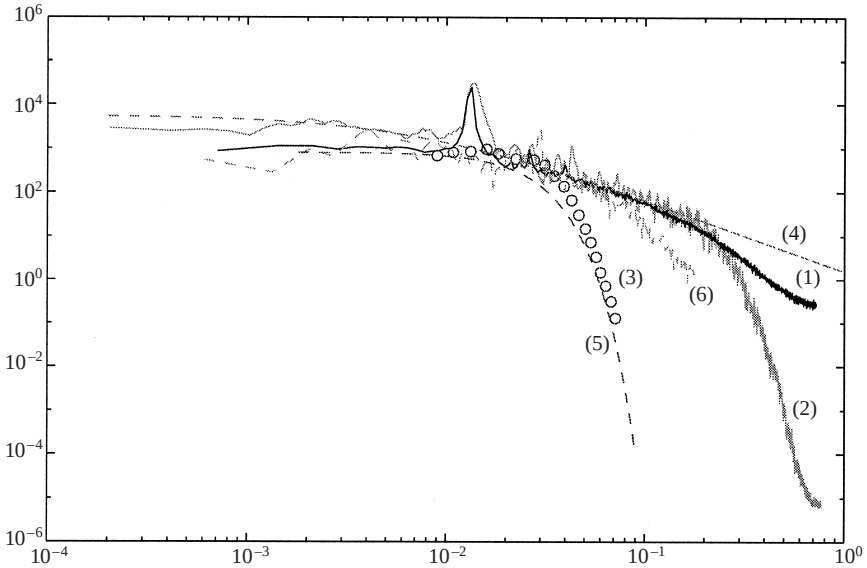

FIGURE 24. One-dimensional streamwise velocity spectrum (Kolmogorov scaling) in the near wake of flow past a cylinder at $Re = 3900$ (normalized energy versus $k_1\eta$): (1) experiment Ong & Wallace; (2) low-resolution DNS; (3) Beaudan & Moin; (4) equation (5.1); (5) equation (5.2); (6) Mittal & Moin.

is dominated by vortex shedding is not. The surprising good agreement between the low-resolution predictions and the experimental results suggest that most of the contribution to Reynolds stress and momentum fluxes comes from the larger structures of the flow. This statement is also supported by the LES studies presented here. Both our spectral LES and the LES runs of Moin and collaborators obtained good statistics, although the small-scale activity and the associated inertial range was not captured in the over-dissipative simulations. From the dynamical systems point of view, we could argue that there is a finite, relatively small number of degrees of freedom that governs the dynamics of the near wake in the vortex-shedding-dominated regions.

To investigate this hypothesis rigorously, in the following we quantify the contribution from the coherent structures using first a phase-averaging technique, and second a decomposition of the flow into its most energetic components.

6.1. *Phase-averaged contributions*

We have implemented a modified version of the phase-averaging technique used in the experiments of Matsumura & Antonia (1993) in order to quantify the contribution from the coherent structures. In the experiment they used the local cross-flow (filtered) velocity at the centreline as criterion for detecting the generally variable Strouhal period. However, it is more accurate and computationally more convenient to use the lift as criterion for the Strouhal period detection, so that there is a common reference for all points in the domain unlike the method of Matsumura & Antonia (1993). We found in our numerical experiments that if a fixed Strouhal period is used, corresponding to the measured value $St = 0.21$, then the phase-averaged contribution tends to zero for a long time averaging over 100 shedding cycles. If short time averaging is used instead, the distributions look reasonable but are not correct as they are not converged. This is why we need to perform phase averaging with the

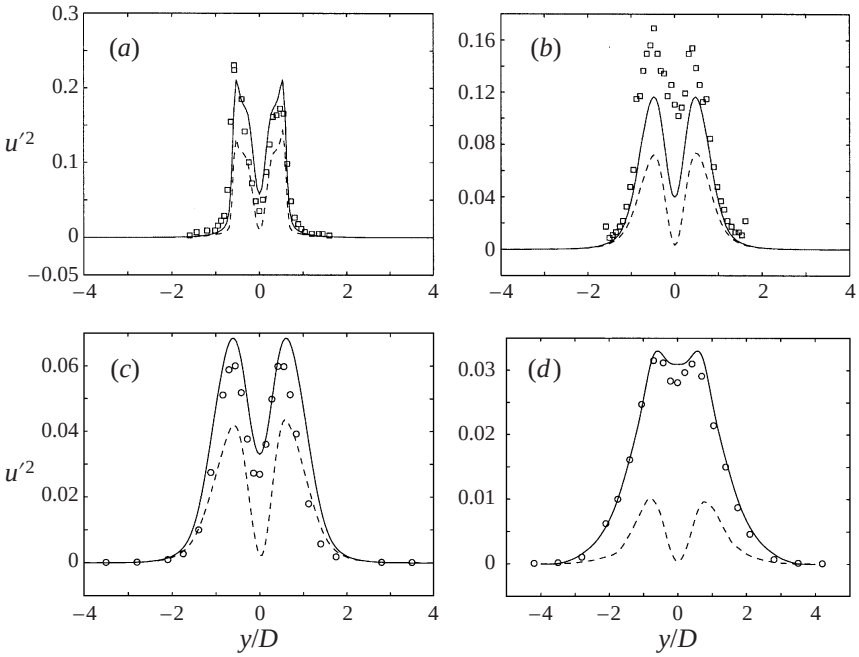

FIGURE 25. Global and coherent streamwise normal Reynolds stresses at $x/D = 1.06$ (*a*), 2.02 (*b*), 3.0 (*c*), 10.0 (*d*). Squares denote experimental data of Lourenco & Shih, circles denote experimental data of Ong & Wallace, solid line global component, and dashed line coherent component.

actual variable Strouhal frequency. To this end, the phase ϕ in our simulations is then calculated from the time history of the lift coefficient $C_L(t)$, which is fairly smooth, as

$$\phi = \pi \frac{t - t_{1,i}}{t_{2,i} - t_{1,i}} \quad \text{for } t_{1,i} \leqslant t \leqslant t_{2,i},$$

$$\phi = \pi \frac{t - t_{2,i}}{t_{1,i+1} - t_{2,i}} + \pi \quad \text{for } t_{2,i} \leqslant t \leqslant t_{1,i+1},$$

where $t_{1,i}$ and $t_{2,i}$ correspond to times when $C_L = 0$, $\mathrm{d}C_L/\mathrm{d}t > 0$ and $C_L = 0$, $\mathrm{d}C_L/\mathrm{d}t < 0$, respectively. Also, the interval $2(t_2 - t_1) = St^{-1}$ (in non-dimensional units), where St represents an averaged Strouhal number value. The entire interval was divided into 60 equal intervals, exactly as in the experiments, and a total of more than 33 periods was used for the averaging. This is lower than the 900 periods used in the experiments, but still sufficient to obtain converged results. Indeed, we found via numerical experiments that using relatively short phase averaging (less than 10 shedding cycles), the phase-averaged quantities are largely over-predicted. In the following, we decompose an instantaneous quantity

$$q(x, y, z, t) = \overline{q} + \tilde{q} + q_r$$

following the triple decomposition of Reynolds & Hussain (1972) into global, coherent, and random contributions, respectively.

For this analysis we use data from the DNS of Case III. In figure 25 we plot the normal (streamwise) Reynolds stress using both the conventional or global averaging quantity $\overline{q's'}$ as well as the phase-averaged quantity $\overline{\tilde{q}\tilde{s}}$, as outlined above. We note that the phase-averaged normal streamwise stress is zero at the centreline with maxima

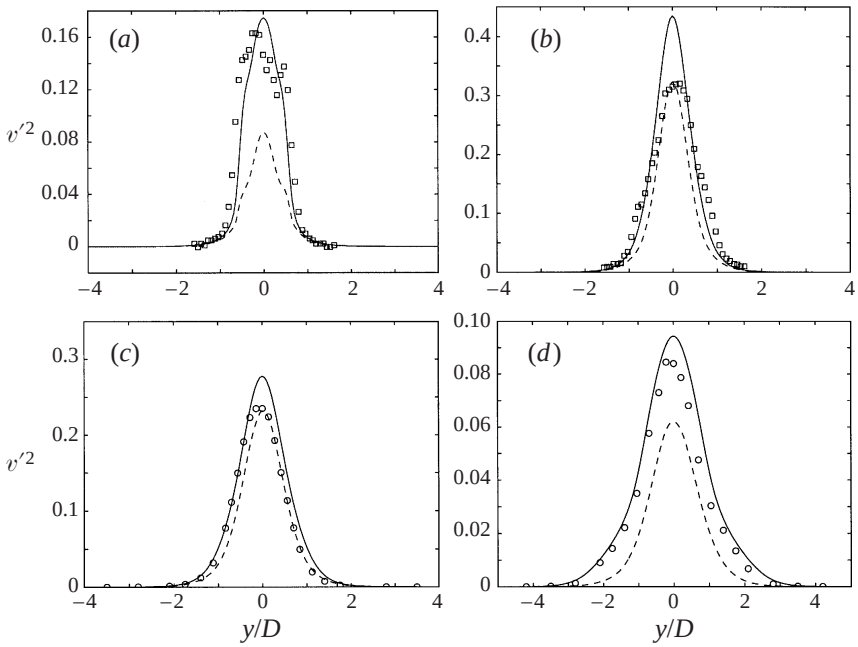

FIGURE 26. As figure 25 but for cross-flow normal Reynolds stresses.

on each side, in agreement with the experiments of Matsumura & Antonia (1993) at $Re = 5830$. We also see that as we move downstream the overall contribution of $\widetilde{u'^2}$ to total Reynolds stress is decreasing monotonically for $x/D \geqslant 2$. In contrast, the coherent contribution to the normal cross-flow Reynolds stress increases as we move downstream. This is shown in figure 26 where we plot the global Reynolds stress and the coherent component $\widetilde{v'^2}$. A conclusion reached in the experimental work of Matsumura & Antonia (1993) was that at locations $x/D = 10$ and farther downstream where they obtained measurements, the coherent contribution to the transport of $\overline{v'^2}$ is higher than that of $\overline{u'^2}$. This has been verified in our simulations, e.g. by comparing figures 25 and 26 at $x/D = 10$ (plots at $x/D = 7$ are very similar). However, this conclusion is not valid in the very near wake, where the relative coherent contribution is higher for the streamwise component. Detailed percentages at various locations for both normal stresses are shown in table 2. Here we have adopted the metric used by Matsumura & Antonia to quantify this contribution defined by

$$S_c = \int |\overline{\tilde{q}'\tilde{s}'}|\,\mathrm{d}y, \quad S_g = \int |\overline{q's'}|\,\mathrm{d}y,$$

and the ratio S_c/S_g of coherent to global contributions.

We have also included in table 2 the percentage of the coherent contribution to the global Reynolds stress $\overline{u'v'}$ and have plotted corresponding profiles at representative locations in figure 27. First, for the locations downstream at $x/D = 10$ (and similarly for $x/D = 7$) the Reynolds stress distribution looks very similar to the one obtained experimentally by Matsumura & Antonia (1993). In particular, at $y/D \approx 1.5$ there is a tendency for the coherent contribution to reduce the level of global Reynolds stress. This behaviour is location-dependent as first noted by Matsumura & Antonia (1993) and confirmed in our DNS. In the very near wake, for example at $x/D = 1.06$,

x/D	q	s	S_c	S_g	$\%(S_c/S_g)$
1.06	u'	u'	0.121	0.207	58.6
	v'	v'	0.084	0.178	47.1
	u'	v'	0.037	0.044	84.0
1.54	u'	u'	0.142	0.238	59.2
	v'	v'	0.271	0.404	67.2
	u'	v'	0.078	0.0117	68.0
2.02	u'	u'	0.107	0.181	59.0
	v'	v'	0.303	0.446	67.9
	u'	v'	0.069	0.105	66.0
5.0	u'	u'	0.059	0.125	47.2
	v'	v'	0.211	0.302	72.3
	u'	v'	0.008	0.026	33.0
7.0	u'	u'	0.041	0.114	35.7
	v'	v'	0.171	0.260	65.7
	u'	v'	0.006	0.020	30
10.0	u'	u'	0.022	0.098	22.5
	v'	v'	0.106	0.209	50.9
	u'	v'	0.004	0.015	28.0

TABLE 2. Contribution of the coherent structure S_c compared to the global quantity S_g at different locations.

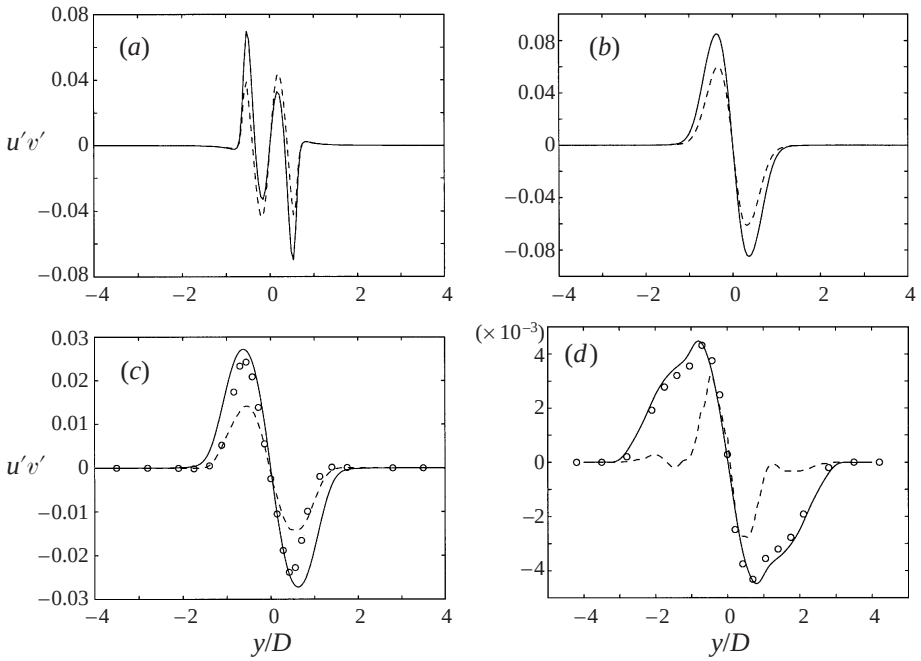

FIGURE 27. Global and coherent Reynolds stresses at $x/D = 1.06$ (a), 2.02 (b), 3.0 (c), 10.0 (d). Circles denote experimental data of Ong & Wallace, solid line global component, and dashed line coherent component.

we see in figure 27 that the coherent contribution seems to be larger than the value of the conventional global Reynolds stress. This occurs at the locations $y/D = \pm 0.5$ which correspond to the approximate location of the shear layers developing on the two sides of the cylinder. In general, the coherent contribution constitutes a large percentage of the total Reynolds stress with the same sign.

6.2. *Proper orthogonal decomposition*

In addition to the analysis presented above, we can also employ the method of proper orthogonal decomposition (POD) (Lumley 1981; Aubry, Guyonnet & Stone 1991) or the computationally more convenient method of empirical eigenfunction (Sirovich 1987). A rigorous presentation of the method can be found in Bekooz, Holmes & Lumley (1993), so here we briefly review the main concept as applied to the cylinder turbulent wake.

The POD procedure identifies the most energetic contributions and obtains the spatial structure of the corresponding modes. Application of this method requires *a priori* storage of velocity fields (snapshots) of the time-dependent flow – they constitute the data ensemble. The modes obtained are simply the eigenfunctions of the velocity autocorrelation operator and form an orthogonal set. Specifically, in order to obtain the eigenfunctions, ψ_i, corresponding to a spatio–temporal velocity field u, we seek to maximize the mean-square fluctuation of the function ψ_i, i.e.

$$\frac{\langle (u, \psi_i)(u, \psi_i) \rangle}{(\psi_i, \psi_i)} = \lambda_i \tag{6.1}$$

where $\langle\ \rangle$ is the ensemble averaging operation which is taken to be the time average for spatio–temporal data, and $(,)$ is the standard inner product. Maximization of the above quantity in equation (6.1) is a classical problem of variational calculus and leads to

$$\int \langle u(x)u(x') \rangle \phi_i(x')\, \mathrm{d}x' = \lambda_i \phi_i(x)$$

where $\phi_i = \psi_i$ is the solution (eigenfunction) with corresponding eigenvalue λ_i. These empirical eigenfunctions are ordered according to their decreasing energy content, which with the appropriate normalization is represented by λ_i. Any member of the ensemble can then be expanded as

$$u(x, t) = \sum_{i=1}^{M} a_i(t)\phi_i(x),$$

where M is the number of snapshots. The following orthogonality relations thus holds:

$$\langle a_i(t), a_j(t) \rangle = \delta_{ij}\lambda_i,$$

where δ_{ij} is the Kronecker delta. Note that this procedure can be performed based on the instantaneous velocity or vorticity vector fields obtained from DNS or on the corresponding fluctuations after we subtract the ensemble-averaged field; similar results are obtained in either case, as has shown by Bangia *et al.* (1997).

Here we have performed the POD analysis for the instantaneous vorticity fields at $Re = 3900$. In particular, we first analyse the time-dependent two-dimensional Fourier coefficients and here we present results for the zero (mean) as well as the first mode. As discussed in Bekooz *et al.* (1993), in the homogeneous direction the POD eigenfunction reduces to a Fourier mode. We can then perform the POD analysis

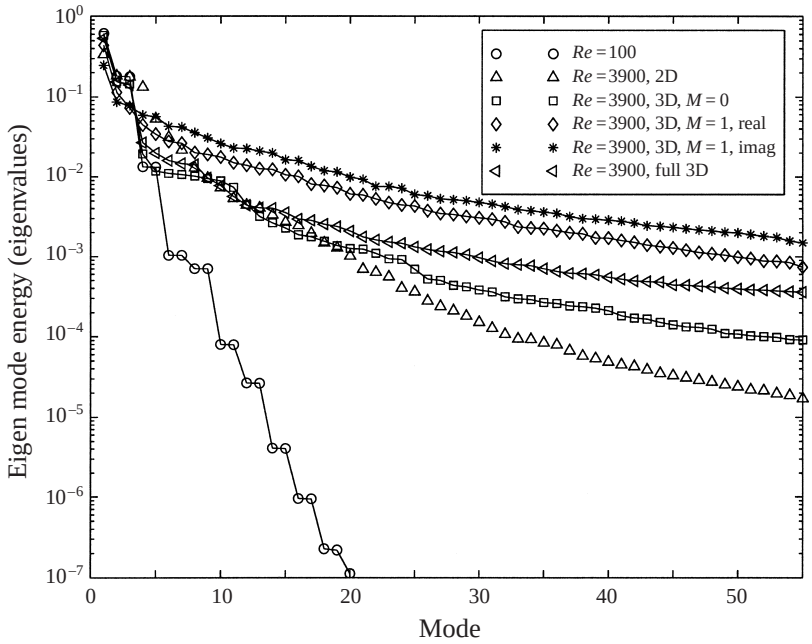

FIGURE 28. Eigenvalues from the POD analysis for vorticity fields corresponding to $Re = 100$, 3900 (two dimensions) and $Re = 3900$ (three dimensions). All 3D data are from Case III.

for the corresponding Fourier coefficients, which in our case are vector fields in the (x, y)-plane. For reference, we also performed POD analysis for a corresponding two-dimensional flow at $Re = 100$ and $Re = 3900$, and also POD analysis for the entire three-dimensional field without the homogeneous assumption invoked along the span. However, we doubled the number of snapshots by employing symmetry conditions along the cross-flow direction.

In figure 28 we plot the eigenvalues obtained from the POD analysis for the spanwise vorticity fields from two- and three-dimensional simulations. For the two-dimensional case at $Re = 3900$ we used 79 snapshots extending over two shedding cycles, whereas for the three-dimensional case with the Fourier decomposition in the span we used 84 snapshots over 7 shedding cycles. For the full three-dimensional analysis we used 55 snapshots over more than 2 shedding cycles. The main conclusion from this plot is that even for the turbulent wake, an initial rapid convergence is obtained with most of the energy captured with less than 20 modes. In fact, the energy decay of the mean vorticity field for $M = 0$ mode and the two-dimensional field are quite similar up to 20 modes whereas the decay of the $M = 1$ mode, which has been separated into real and imaginary parts, is slightly slower. We also note that, unlike the eigenvalues at $Re = 100$, which appear in pairs, this is not the case at higher Reynolds number.

Next, we examine the structure of the first few eigenmodes of the spanwise vorticity for the zeroth mode ($M = 0$). In figure 29 we plot the first and second mode corresponding to U-shape (Case II) and V-shape (Case III) solutions. We only plot the very near wake where differences are pronounced as has already been discussed. It is clear from these plots that the time-averaged shear layers are longer for the U-shape solution and that the formation length is longer. Farther downstream such differences are not noticable so we only present results for the V-shape solution in

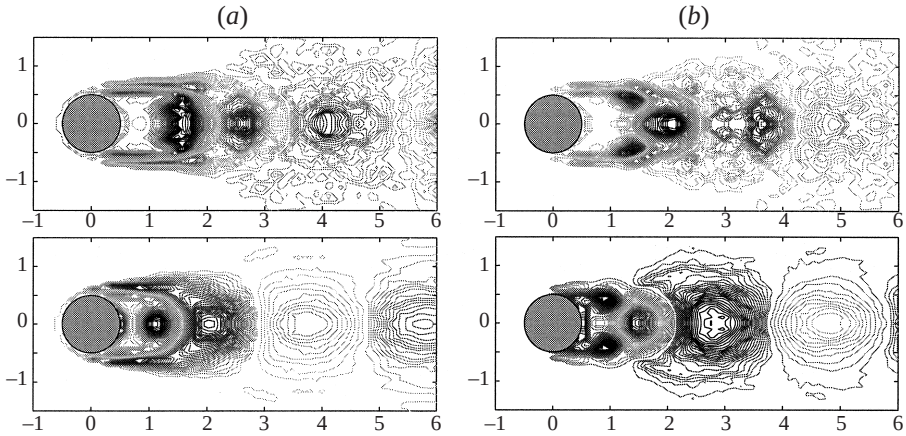

FIGURE 29. Vorticity eigenfunctions corresponding to first (*a*) and second (*b*) modes. The data show the very near wake corresponding to a U-shape (top; long formation length, Case II) and a V-shape (bottom; short formation length, Case III) for each mode.

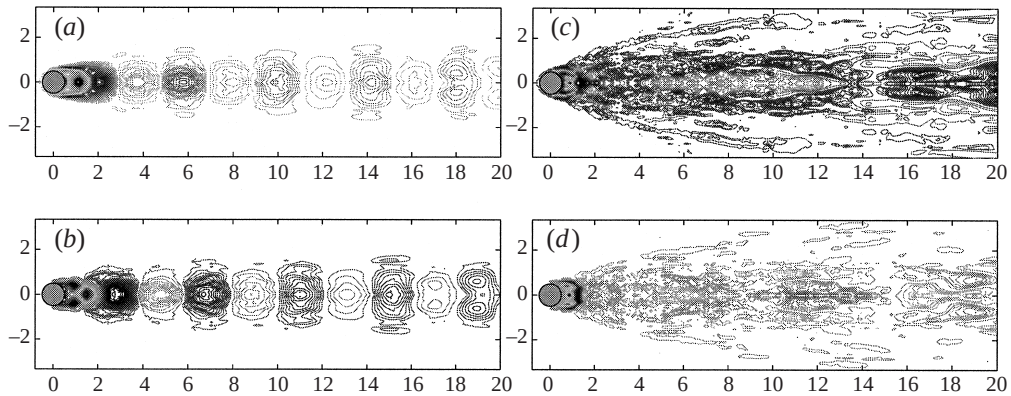

FIGURE 30. Eigenmodes ((*a*) first, (*b*) second, (*c*) third, (*d*) fourth) from the POD analysis for spanwise vorticity at $Re = 3900$ for the mean flow $M = 0$ (V-shape solution).

figure 30. The first pair is very similar to the first pair of empirical eigenfunctions of a laminar wake first computed in Deane *et al.* (1991), but the next pair contains small scales unlike the laminar wakes. This first pair is very different, however, from the first pair of the corresponding two-dimensional flow at $Re = 3900$.

Finally, in figure 31 we plot the reconstruction of the vorticity contour; the contour of the full simulation is plotted in figure 31(*a*). We first use only two eigenmodes and we see that the vortex street is correctly captured, and that with 11 or 13 eigenmodes the majority of small scales are also captured.

7. Summary and discussion

We have performed systematic direct and large-eddy simulations of turbulent flow past a circular cylinder at $Re = 3900$ in order to resolve conflicting experimental and numerical results available in the literature. A new finding is that two converged states, distinctly different, were obtained in the very near wake (up to about three cylinder diameters) but then converge downstream. This reflects the dynamics of

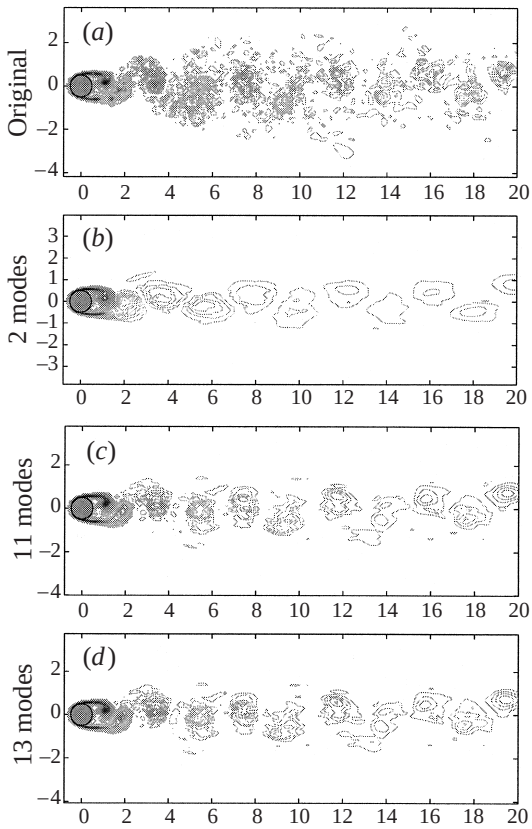

FIGURE 31. Reconstruction of instantaneous span-averaged vorticity from 2 (*b*) and 11–13 (*c*, *d*) eigenmodes. (*a*) The contour obtained from the full simulation which is used in the projection. (Case II).

the flow, which is governed by the shear layers in the very near wake which are quite sensitive to allowable disturbances, and of the vortex shedding in the region downstream which is more robust.

The first state corresponds to the mean streamwise velocity profile having a U-shape at about one diameter downstream, whereas the second state corresponds to a V-shape. The U-shape solution emerges if the background fluctuations are relatively low or the spanwise extent of the domain is small, e.g. $L_z/D = \pi$. This solution was obtained in the LES studies of Moin and co-workers (Beaudan & Moin 1994; Mittal & Moin 1997; Kravchenko & Moin 1998) who employed the aforementioned value of cylinder span in all their simulations. The spectral DNS presented here, also converge to a U-shape state for the same domain, but they converge to a V-shape state for wider computational domains. These findings explain the great uncertainty regarding the value of the formation length, especially in this Reynolds number regime (see Noca *et al.* 1998).

We have also implemented an LES formulation appropriate for high-order methods with sub-cell resolution. In order to study the effect of subfilter dissipation on the solution type we varied the Smagorinsky constant from a low to a larger value. Figure 32 shows the effect of the subfilter viscosity on the streamwise turbulence intensity at $x/D = 1.06$ for $-1.5 < y/D < 1.5$. The streamwise turbulence intensities

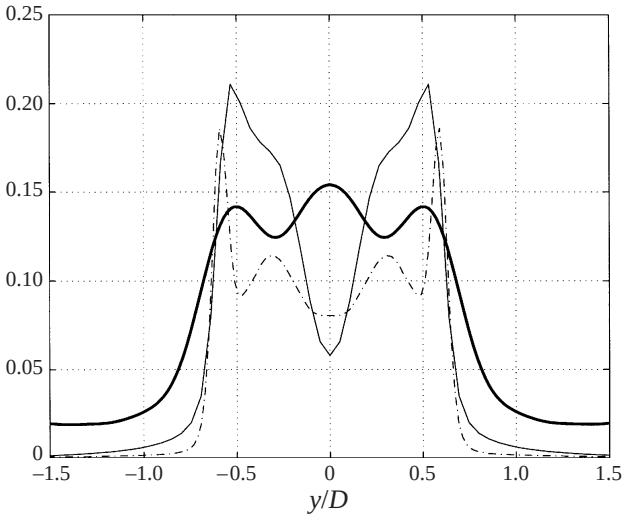

FIGURE 32. Effect of subfilter scale model on r.m.s. streamwise velocity predictions at $x/D = 1.06$: the solid thick line represents the ratio of subfilter viscosity to kinematic viscosity for Case IV; the solid thin line represents Case III (no subfilter); the thin dash-dot line corresponds to Case IV (low subfilter).

are superimposed on the ratio of subfilter scale viscosity to the kinematic viscosity. Cases III and IV (see table 1) are presented, which have the same resolution and computational domain. The difference in r.m.s. is solely due to the subfilter-scale model. Apart from an overall reduction in turbulence intensities from Case III to Case IV, a correlation is evident between the peaks of the subfilter viscosity and the 'valleys' on the turbulence intensities of Case IV. Also, given that the two highest peaks are indicative of the shear layer, then the subfilter model is reducing the width of these shear layers.

On the question of the turbulence state in the near wake, we have found that the energy spectrum has a substantial inertial subrange at $Re = 3900$, in agreement with the experiments. All spectral DNS performed captured that inertia range quite accurately. However, only the LES with the smaller subfilter dissipation also reproduced the inertial range. The higher-dissipation LES gave a result very close to an earlier LES by Mittal & Moin (1997). This result is consistent with the more recent results of Kravchenko & Moin (1998) who obtained the correct inertial range using high-order discretization. It appears that excessive dissipation due to either the subfilter model or the discretization can suppress significantly the small-scale fluctuations, altering greatly the inertial range. This does not necessarily imply that the prediction of the velocity field is erroneous, as the cylinder flow is dominated by the robust vortex shedding process. However, there are subtle differences in the very near wake as discussed above.

The surprising result is that a simulation employing only two modes in the span without a subfilter model was able to predict both mean and r.m.s. velocities with reasonable accuracy. For example, the drag coefficient predicted with $M = 2$ modes is $C_D = 0.981$ in agreement with the experimental value 0.98 ± 0.05 (Norberg 1987). For reference, the C_D value obtained in the LES of Beaudan & Moin (1994) is 1.0 and the corresponding two-dimensional value reported in Beaudan & Moin (1994) is $C_D = 1.74$. In fact, the results from the LES study of Beaudan & Moin (1994) are comparable in quality with the low-resolution DNS results. Both simulations provide

Case	K	P	M	$L_z/(\pi D)$	c_s	C_p	St	Bubble length/D	Solution type
VI	1622	8	32	1.5	0.0	1.06	0.212	0.96	V-type
VII	902	10	32	1.0	0.0	0.85	0.202	1.45	U-type
VIII	902	9	32	1.0	0.0	0.90	0.211	1.3	V-type
IX	902	8	32	2.0	0.0	1.01	0.211	1.01	V-type
X	902	8	8	2.0	0.0	1.08	0.18	1.03	V-type
XI	902	8	8	1.0	0.0	1.11	0.192	0.91	V-type
XII	902	8	16	1.0	0.0	1.02	0.21	1.01	V-type
XIII	902	6	16	1.0	0.0	1.08	0.202	0.93	V-type
XIV	902	10	8	0.5	0.0	1.2	0.206	0.77	V-type
XV	902	8	8	0.5	0.0	1.15	0.208	0.84	V-type
XVI	902	6	4	1.0	0.0	1.14	0.17	0.99	V-type
XVII	902	7	8	1.0	0.0	1.1	0.19	0.94	V-type
XVIII	902	4	2	0.5	0.0	1.03	0.213	0.78	V-type
XIX	902	7	2	0.5	0.0	1.65	0.177	0.48	V-type
XX	902	6	2	0.5	0.0	0.93	0.215	1.01	V-type
XXI	902	9	—	—	0.0	2.07	0.268	0.0	V-type

TABLE 3. Summary of simulations for resolution studies. Cases I–V can be found in table 1 in the main text.

reasonably accurate velocity profiles despite the erroneous prediction of the energy spectrum.

To investigate this result, which has also been realized in turbulent channel flow (Zores 1989) but has remained largely unnoticed, we performed a systematic study to quantify the contribution from the coherent motion to the mean flow and the Reynolds stresses. We first employed a modification of a phase-averaging technique used in the experimental studies of Matsumura & Antonia (1993) for the intermediate wake, and then we analysed the most energetic modes using the proper orthogonal decomposition approach. The results from both approaches suggest that the turbulent near wake behaves as a dynamical system of relatively low dimensionality. In particular, a dynamical model that employs 10 to 20 most energetic modes in the (x, y)-plane and 2 to 4 Fourier modes along the span could be a reasonably accurate model for the flow past a cylinder in the Reynolds number range below 5000 as studied here. Similar conclusions were reached in Deane *et al.* (1991), where only 4 POD modes were sufficient to construct Galerkin models for the unsteady laminar wake. Future work will rigorously address the validity of such a hypothesis.

This work was supported partially by ONR and NSF. Work on numerical methods and on parallel algorithms developed for the simulations presented in this paper were supported under different grants by AFOSR and DOE. The computations were performed on the IBM SP2 at Maui High Performance Computing Center (MHPCC), at the NCSA University of Illinois (Urbana-Champaign) and at Brown University. We would like to thank Dr L. Ong, Professor J. Wallace and Professor C. H. K. Williamson for providing their experimental data in tabular form. We also like to thank Professor P. Moin and Professor R. Mittal for providing useful comments of an earlier version of this work.

Appendix A. Resolution studies

A summary of 21 simulations is presented in tables 1 and 3, using different polynomial order P, different Fourier modes M, different meshes K, and different

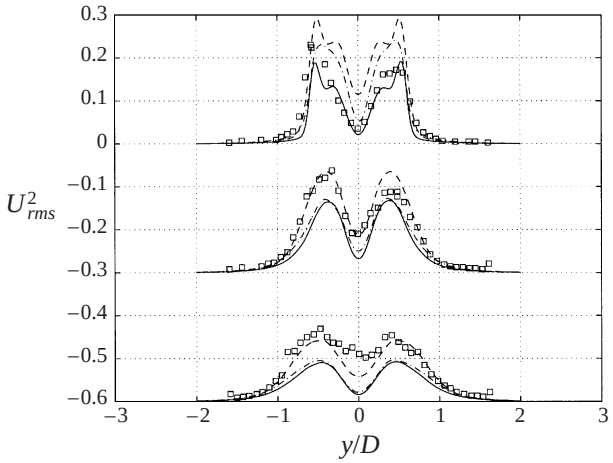

FIGURE 33. DNS r.m.s. streamwise velocity predictions at $x/D = 1.06, 1.54, 2.02$. Case XII (solid line), Case XV (dash-dot line) and Case IX (dashed line). Squares are data of Lourenco & Shih.

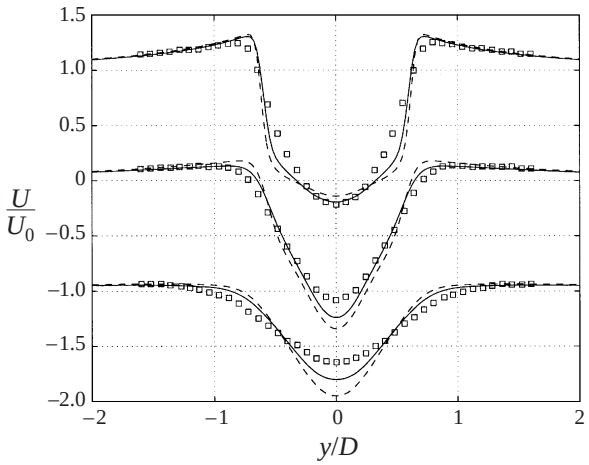

FIGURE 34. DNS mean streamwise velocity predictions at $x/D = 1.06, 1.54, 2.02$. Case VIII (solid line) and Case VII (dashed line). Squares are data of Lourenco & Shih.

computational domains (L_z). In all the high-resolution DNS, the far wake was rather insensitive to resolution changes, while the very near wake was quite sensitive to spanwise length, spanwise resolution, and p-refinement. In the following we summarize the main effects we observed in these resolution studies:

Effect of span: We increase the spanwise length scale L_z, with P and effective spanwise resolution (M/L_z) remaining constant. The cases we consider are denoted in table 3 by IX, XII and XV. At $x/D = 1.06$, the velocity profile becomes wider (i.e. more U-shaped), and the bubble length increases, in the order of $L_z/D = \pi/2, 2\pi, \pi$. Concerning the r.m.s. streamwise velocities (figure 33), at $x/D = 1.06$, the $L_z/D = 2\pi$ and $L_z/D = \pi$ cases have similar profiles, with sharp peaks, with the former having higher values than the latter. The $L_z/D = \pi/2$ case has turbulence intensities in between the other two cases, with a 'thicker' profile. At $x/D = 1.54, 2.02$, the $L_z/D = 2\pi$ case is higher than the $L_z/D = \pi, \pi/2$ cases, which are similar.

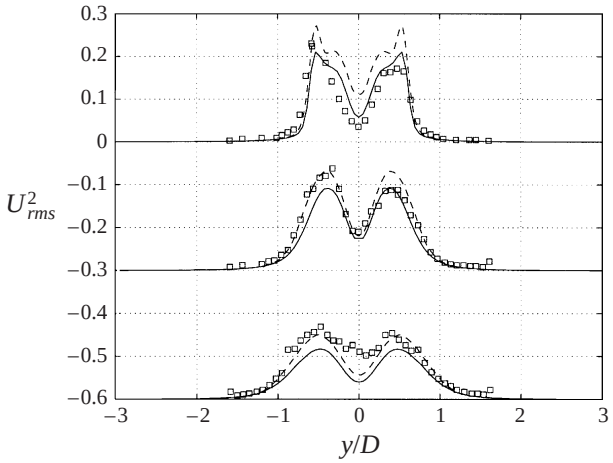

FIGURE 35. DNS r.m.s. streamwise velocity predictions at $x/D = 1.06$, 1.54, 2.02. Case I (solid line) and Case IX (dashed line). Squares are data of Lourenco & Shih.

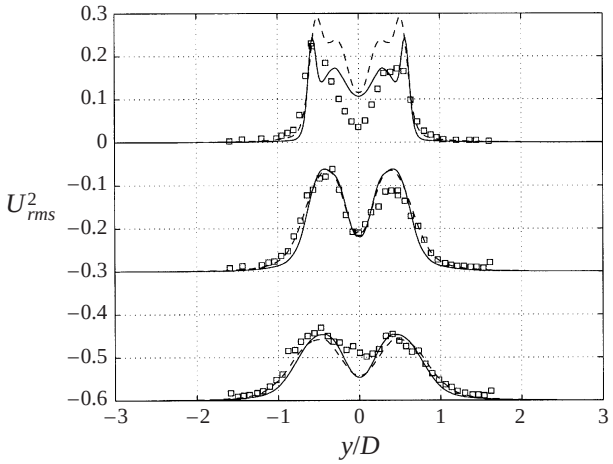

FIGURE 36. DNS r.m.s. streamwise velocity predictions at $x/D = 1.06$, 1.54, 2.02. Case III (solid line) and Case VI (dashed line). Squares are data of Lourenco & Shih.

Effect of p-refinement: We increase the spectral order P, with the computational domain and spanwise resolution constant (Cases VII, VIII). The U-shape profile is accentuated with increasing P, with the bubble length also increasing (figure 34). The cross-flow velocities are rather insensitive to increases in P.

Effect of total refinement: We increase P and spanwise resolution M for $L_z = 2\pi$ (Cases I, IX). For the mean streamwise velocities, the increase in resolution increases the width of the profile at $x/D = 1.06$, while the streamwise turbulence intensities (figure 35) drop with increasing resolution at $x/D = 1.06$.

Effect of h-refinement: We performed an h-refinement in the shear layer region from $k = 902$ to 1622 elements, with constant computational domain (Cases III, VI). The velocity profiles are insensitive to the increase in resolution, maintaining a V-shape profile, while the r.m.s. streamwise predictions (figure 36) increase in magnitude.

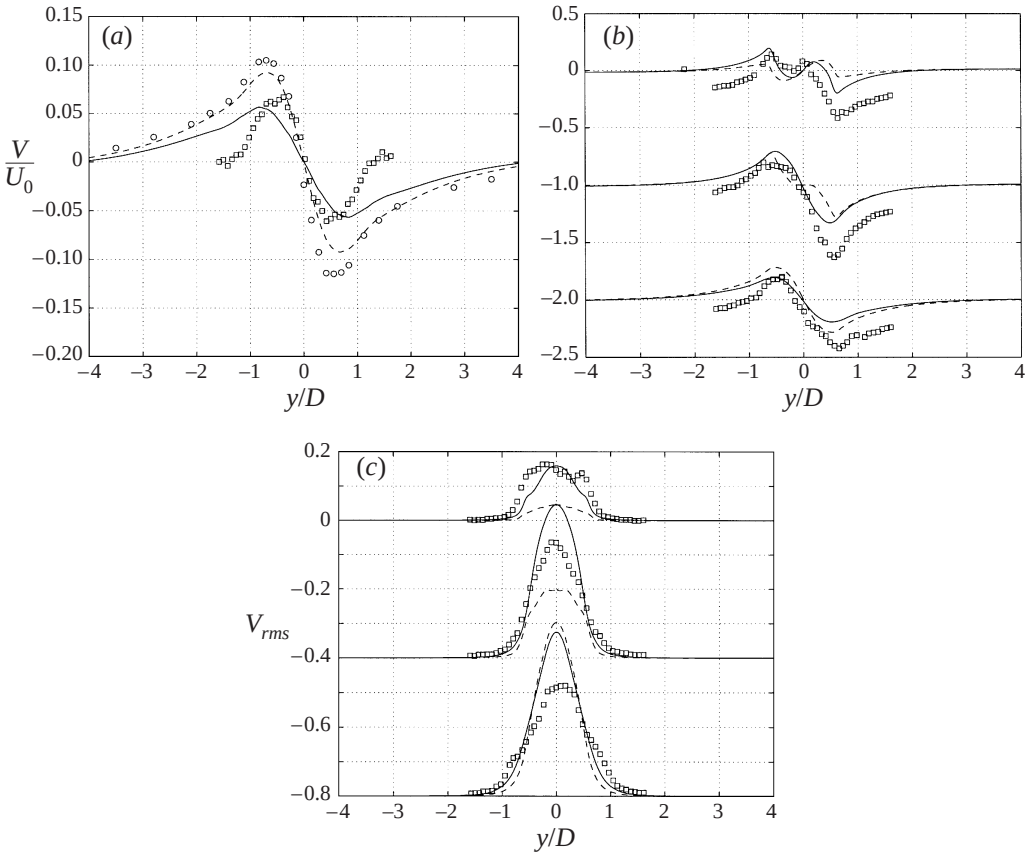

FIGURE 37. DNS mean cross-flow velocity predictions at (*a*) $x/D = 3.0$, (*b*) $x/D = 1.06$, 1.54, 2.02; and (*c*) DNS r.m.s. cross-flow velocity predictions at $x/D = 1.06$, 1.54, 2.02. Case I (wide domain – solid line) and Case II (narrow domain – dashed line). Squares are data of Lourenco & Shih; circles are data of Ong & Wallace.

Appendix B. Comparison of cross-flow velocity

We present here comparison of cross-flow velocity profiles and cross-flow turbulence intensities. DNS simulations (Cases I, II; see table 1) show the effect of spanwise length, while LES simulations (Cases III, IV, V; see table 1) show the effect of subfilter dissipation on cross-flow profiles. The simulations are compared to the experimental data of Lourenco & Shih and Ong & Wallace. For the former experiment, according to Beaudan & Moin, symmetry errors in Reynolds stresses, streamwise and vertical velocities indicate that the errors in the cross-flow mean velocity are comparable to the cross-flow velocities themselves over the entire domain of measurement. For the streamwise velocity past one cylinder diameter symmetry errors stand at 5% of the maximum local velocity, while Reynolds shear stresses have a 20% error for $x/D < 2$ and for $2.5 < x/D < 4$ the error is around 30%. For the latter experiment, Ong & Wallace provided experimental uncertainties of 2% for mean velocities and 3% on Reynolds stresses, with the symmetry errors being negligible compared to these experimental uncertainties. However, we have already mentioned that their streamwise velocity taken at centreline points has an erroneous pronounced peak at the Strouhal frequency.

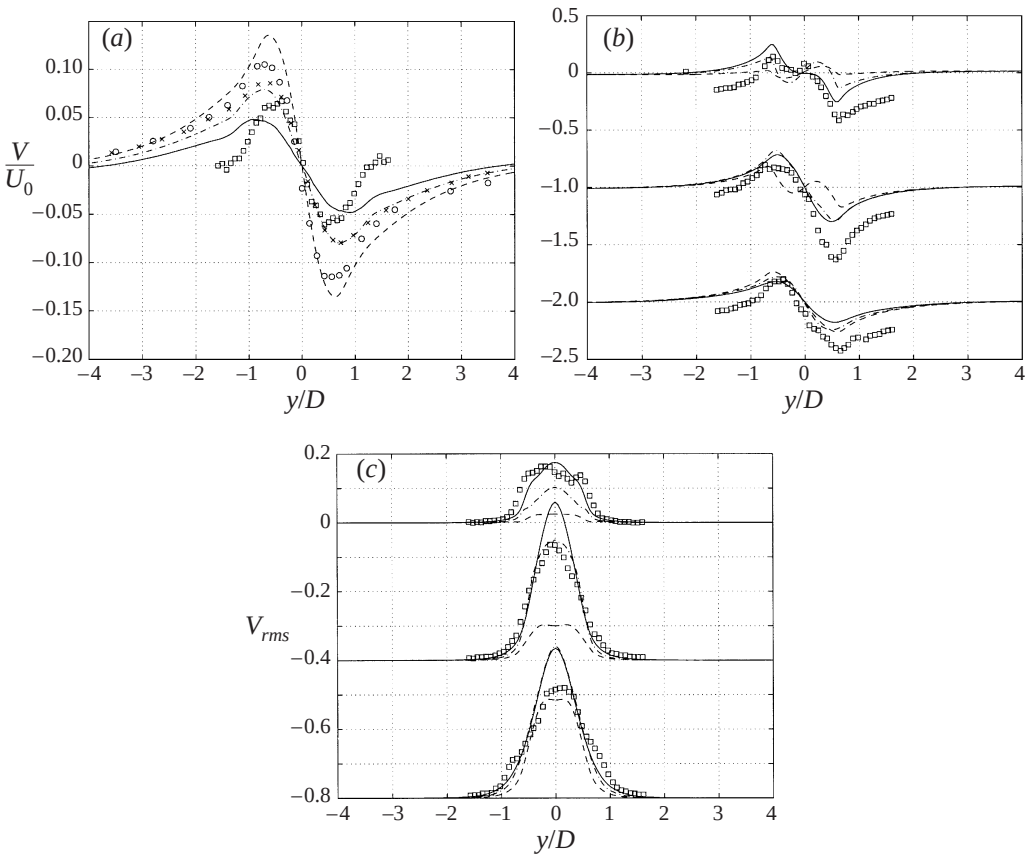

FIGURE 38. LES mean cross-flow velocity predictions at (*a*) $x/D = 3$, (*b*) $x/D = 1.06$, 1.54, 2.02 (*c*) LES r.m.s. cross-flow velocity predictions at $x/D = 1.06$, 1.54, 2.02. Case III (no subfilter – solid line), Case IV (low subfilter – dash-dot line), and Case V (high subfilter – dashed line). Squares are data of Lourenco & Shih; circles are data of Ong & Wallace; crosses are LES of Mittal & Moin.

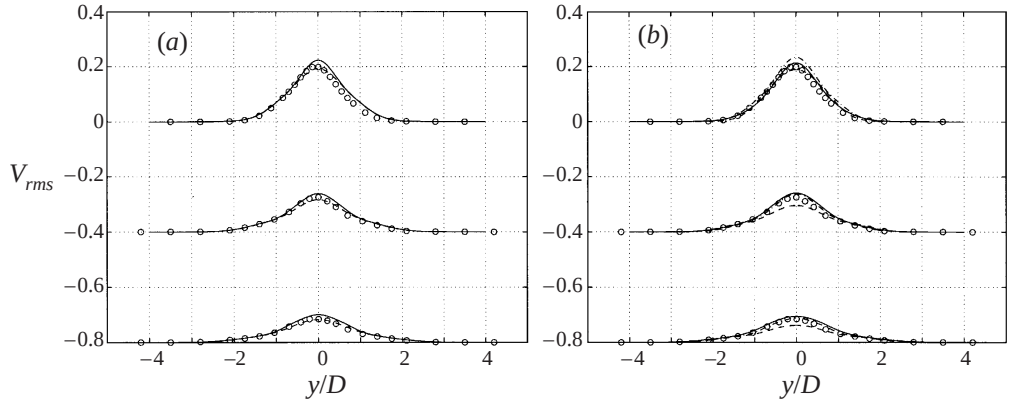

FIGURE 39. Profiles of r.m.s. cross-flow velocity at $x/D = 4$, 7, 10. (*a*) DNS comparison for Case 1 (solid line) and Case II (dashed line). (*b*) LES comparison for Case III (solid line), Case IV (dash-dot line), and Case V (dashed line). Circles denote experimental data of Ong & Wallace at $Re = 3900$.

The very near wake: U-shape versus V-shape

Comparisons of DNS predictions with experimental data for $x/D \leqslant 3$ at $Re = 3900$ are first presented, concentrating on mean velocities and turbulence intensities. It is note worthy that the experiments of Lourenco & Shih, and Ong & Wallace do not match each other, as shown for $x/D = 3$ in figure 37(*a*): Cases I and II are also plotted. Apart from a difference in the maximum magnitude of velocity, the spread of the Ong & Wallace profile is larger, with asymmetries evident in both sets of experimental data. The DNS calculations follow a similar pattern to the Ong & Wallace experiment, with the magnitude of velocity decreasing with decreasing spanwise length (Case I versus Case II).

In the very near wake, only the experimental data of Lourenco & Shih are available, and figure 37(*b*) compares Cases I and II. Although there is a distinct difference in profile (U-shape versus V-shape) in the streamwise velocities at $x/D = 1.06$, the cross-flow velocity profiles exhibit similar behaviour, with different magnitudes. Similar behaviour is noted for the cross-flow turbulence intensities at the same positions (figure 37*c*). The lack of symmetry in the experimental data extends to this quantity, with the mean cross-flow velocity reaching a non-zero value away from the cylinder centreline.

Comparison of the effect of subfilter dissipation (Cases III, IV, and V) is also presented, first at $x/D = 3.0$ (figure 38*a*). The increase in subfilter dissipation leads to an increase in cross-flow velocity magnitude. Similar behaviour is noted at $x/D = 2.02$ (figure 38*b*). At $x/D = 1.06$, the mean velocity profiles are different, depending on the degree of U-shape profile of the streamwise velocity profiles (figure 7). The velocity changes from a profile similar to the experimental result, to an inverted-shape profile, with increasing dissipation. This is directly related to the U- or V-shape profiles, and the decreasing magnitude of cross-flow turbulence intensity (figure 38*c*). At $x/D = 1.54$, the difference is less pronounced, yet still distinct.

Statistics for $x/D \geqslant 3$

Above $x/D > 3.0$, an insensitivity of the mean cross-flow velocities to spanwise length and subfilter dissipation was noted, with the velocities tending to zero. A similar insensitivity is also evident in the turbulence intensities, with the DNS simulations (Cases I and II) closely matching the experimental data of Ong & Wallace (1996) (figure 39). This is also the case for the LES simulations, as shown in figure 39.

REFERENCES

Aubry, N., Guyonnet, R. & Stone, E. 1991 Spatio-teemporal analysis of complex signals: Theory and applications. *J. Statist. Phys.* **64**, 683–739.

Bangia, A., Batcho, P., Kevrekidis, I. & Karniadakis, G. E. 1997 Unsteady two-dimensional flows in complex geometries: Comparative bifurcation studies with global eigenfunction expansions. *SIAM J. Sci. Comput.* **18**, 775–805.

Barkley, D. & Henderson, R. 1996 Three-dimensional Floquet stablity analysis of the wake of a circular cylinder. *J. Fluid Mech* **322**, 215–241.

Beaudan, P. & Moin, P. 1994 Numerical experiments on the flow past a circular cylinder at sub-critical Reynolds nuber. *Tech. Rep.* TF-62, Stanford University, Stanford, CA 94305.

Bekooz, G., Holmes, P. & Lumley, J. 1993 The proper orthogonal decomposition in the analysis of turbulent flows. *Ann. Rev. Fluid Mech.* **25**, 539–575.

Cantwell, B. & Coles, D. 1983 An experimental study of entrainment and transport in the turbulent near wake of a circular cylinder. *J. Fluid Mech.* **136**, 321–374.

Cao, N.-Z. & Aubry, N. 1993 Numerical simulation of wake flow via a redued system. *Proc. ASME Fluids Engineering Conference*, 20–24 June, *Washington DC*.

Chu, D. & Karniadakis, G. E. 1993 A direct numerical simulation of laminar and turbulent flow over riblet-mounted surfaces. *J. Fluid Mech.* **250**, 1–42.

Deane, A., Kevrekidis, I., Karniadakis, G. E. & Orszag, S. 1991 Low-dimensional models for complex geometry flows: Application to grooved channels and circular cylinders. *Phys. Fluids* A **3**, 2337–2354.

Eisenlohr, H. & Eckelmann, H. 1989 Vortex splitting and its consequences in the vortex street of cylinders at low Reynolds number. *Phys. Fluids* A **1**, 189.

Evangelinos, C. 1999 Parallel simulations of vortex-induced vibrations in turbulent flow: Linear and non-linear models. PhD thesis, Brown University.

Frohlich, J., Rodi, W., Kessler, P., Parpais, S., Bertoglio, J. & Laurence, D. 1998 Large eddy simulation of flow around circular cylinders on structured and unstructured grids. In *Notes on Numerical Fluid Mechanics* (ed. E. H. Hirschel). Vieweg.

Gerrard, J. 1978 The wakes of cylindrical bluff bodies at low Reynolds number. *Phil. Trans. R. Soc. Lond.* A **288**, 351.

Gottlieb, D. & Orszag, S. 1977 *Numerical Analysis of Spectral Methods: Theory and Applications.* SIAM-CMBS, Philadelphia.

Hammache, M. & Gharib, M. 1991 An experimental study of the parallel and oblique vortex shedding from circular cylinders. *J. Fluid Mech.* **232**, 567–590.

Henderson, R. & Karniadakis, G. E. 1995 Unstructured spectral element methods for simulation of turbulent flows. *J. Comput. Phys.* **122**, 191.

Huang, L.-S. & Ho, C.-M. 1990 Small scale transition in a plane mixing layer. *J. Fluid Mech.* **210**, 475–500.

Hussain, A. & Hayakawa, M. 1987 Eduction of large-scale organized structures in a turbulent plane wake. *J. Fluid Mech.* **180**, 193–229.

Karamanos, G.-S. 1999 Large eddy simulation using ustructured spectral/hp elements. PhD thesis, Imperial College.

Karniadakis, G. E. & Sherwin, S. 1999 *Spectral/hp Element Methods for CFD*. Oxford University Press.

Karniadakis, G. E. & Triantafyllou, G. 1989 Frequency selection and asymptotic states of laminar wakes. *J. Fluid Mech.* **199**, 441.

Karniadakis, G. E. & Triantafyllou, G. 1992 Three-dimensional dynamics and transition to turbulence in the wake of bluff objects. *J. Fluid Mech.* **238**, 1–30.

Kravchenko, A. & Moin, P. 1998 B-spline methods and zonal grids for numerical simulations of turbulent flows. PhD thesis. Stanford University; *Rep.* TF-73.

Lilly, D. 1967 The representation of small-scale turbulence in numerical simulation experiments. In *Proc. IBM Scientific Computing Symposium on Environmental Sciences, White Plains, NY*, 195.

Liu, C. & Liu, Z. 1997 Advances in DNS/LES. In *Proc. first AFOSR Intl Conf. on DNS/LES*. Greyden Press.

Lumley, J. 1981 In *Transition and Turbulence* (ed. R. Meyer), pp. 215–242. Academic.

Ma, X. 2000 Low-dimensional modeling of turbulent wakes. PhD thesis, Brown University.

Ma, X. & Karniadakis, G. E. 1997 The spectrum of the turbulent near wake: A comparison of DNS and LES. In *Advances in DNS/LES, Proc. first AFOSR Intl Conf. on DNS/LES*, pp. 129–136. Greyden Press.

Mansy, H., Yang, P.-M. & Williams, D. 1994 Quantitative measurements of three-dimensional structures in the wake of a circular cylinder. *J. Fluid Mech.* **270**, 227–296.

Marasli, B. P. & Wallace, J. 1993 A calibration technique f nguyen or multiple-sensor hot-wire probes and its application to vorticity mesurements in the wake of a circular cylinder. *Exps. Fluids* **15**, 209–218.

Matsumura, M. & Antonia, R. 1993 Momentum and heat transport in the turbulent intermediate wake of a circular cylinder. *J. Fluid Mech.* **250**, 277–296.

Mittal, R. 1996 Progress on LES of flow past a circular cylinder. *CTR Annual Research Briefs*, p. 233. Stanford, CA 94305.

Mittal, R. & Moin, P. 1996 Large-eddy simulation of flow past a circular cylinder. In *APS Bulletin*, vol. 41 (9), 49th DFD Meeting.

Mittal, R. & Moin, P. 1997 Suitability of upwind-biased finite difference schemes for large-eddy simulation of turbulent flow. *AIAA J.* **35**, 1415–1417.

Moin, P. & Kim, J. 1982 Numerical investigation of turbulent channel flow. *J. Fluid Mech.* **118**, 341–377.

Monkewitz, P. 1988 The absolute and convective nature of instability in two-dimensional wakes at low Reynolds numbers. *Phys. Fluids* A **31**, 999.

Noca, F., Park, H. & Gharib, M. 1998 Vortex formation length of a circular cylinder ($300 < Re < 4000$) using DPIV. In *Proc. on Bluff Body Wakes and Vortex-Induced Vibration, ASME Fluids Engineering Division, Washington, DC*.

Norberg, C. 1987 Effects of Reynolds number and low-intensity freestream turbulence on the flow around a circular cylinder. *Department of Applied Thermodynamics and Fluid Mechanics, Chalmer University of Technology, Sweden Rep.* **87** (2).

Norberg, C. 1994 An experimental investigation of the flow around a circular cylinder: Influence of aspect ratio. *J. Fluid Mech.* **258**, 287–316.

Ong, L. & Wallace, J. 1996 The velocity field of the turbulent very near wake of a circular cylinder. *Exps. Fluids* **40**, 441–453.

Panton, R. 1997 A Reynolds stress function for wall layers. *Trans. ASME J. Fluids Engng* **119**, 325.

Prasad, A. & Williamson, C. 1997 The instability of the shear layer separating from a bluff body. *J. Fluid Mech.* **333**, 375–402.

Ramberg, S. & Griffin, O. 1976 The effects of vortex coherence, spacing, and circulation on the flow-induced forces on vibrating cables and bluff structures. *Naval Research Lab. Rep.* 7945.

Reynolds, W. & Hussain, F. 1972 The mechanism of an organized wake in turbulent shear flow. Part 3. Theoretical models and comparisons with experiments. *J. Fluid Mech.* **54**, 263–288.

Robichaux, J., Balachandar, S. & Vanka, S. 1999 Three-dimensional Floquet instability in the wake of square-cylinders. *Phys. Fluids* **11**, 560–578.

Sherwin, S. & Karniadakis, G. E. 1995 A triangular spectral element method; applications to the incompressible Navier–Stokes equations. *Comput. Meth. Appl. Mech. Engng* **23**, 83.

Sherwin, S. & Karniadakis, G. E. 1996 Tetrahedral *hp* finite elements: Algorithms and flow simulations. *J. Comput. Phys.* **122**, 191.

Sirovich, L. 1987 Turbulence and the dynamics of coherent structures, Parts I, II and III. *Q. Appl. Math.* XLV, 561–590.

Son, J., & Hanratty, T. 1969 Velocity gradients at the wall for flow around a cylinder at Reynolds numbers from 5×10^3 to 10^5. *J. Fluid Mech.* **35**, 353–368.

Tomboulides, A., Orszag, S. & Karniadakis, G. E. 1993 Direct and large eddy simulations of axisymmetric wakes. In *AIAA Paper* 93-0546.

Townsend, A. 1979 Flow patterns of large eddies in a wake and in a boundary layer. *J. Fluid Mech.* **95**, 515–537.

Triantafyllou, G. & Karniadakis, G. E. 1990 Computational reducibility of unsteady viscous flows. *Phys. Fluids* **2**, 653.

Triantafyllou, G., Triantafyllou, M. & Chryssostomidis, C. 1986 On the formation of vortex streets behind stationary cylinders. *J. Fluid Mech.* **170**, 461–477.

Uberoi, M. & Freymuth, P. 1969 Spectra of turbulence in wakes behind cylinders. *Phys. Fluids* **12**, 1359–1363.

Unal, M. & Rockwell, D. 1988 On vortex shedding from a cylinder. Part 1. The initial instability. *J. Fluid Mech.* **190**, 491–512.

Warburton, T. 1998 Spectral/hp element methods on polymorphic domains. PhD thesis, Brown University.

Williamson, C. 1996 Three-dimensional wake transition. *J. Fluid Mech.* **328**, 345–407.

Williamson, C., Wu, J. & Sheridan, J. 1995 Scaling of streamwise vortices in wakes. *Phys. Fluids* **7**, 2307–2309.

Wu, J., Sheridan, J., Hourigan, K. & Soria, J. 1996 Shear layer vortices and longitudinal vortices in the near wake of circular cylinder. *Exp. Thermal Fluid Sci.* **12**, 169.

Zhou, Y. & Antonia. R. 1993 A study of turbulent vortices in the near wake of a cylinder. *J. Fluid Mech.* **253**, 643–661.

Zores, R. 1989 Numerische untersuchungen mit einem grobauflosenden simulationsmodell fur die turbulente kanalstromung. *Tech. Rep.* Institute fur Theoretische Stromungsmechanik, DLR, Gottingen, Germany.